

Water Resources Research

RESEARCH ARTICLE

10.1029/2018WR024083

Key Points:

- Scaling laws based on flow patterns simulated by the 2-D Shallow Water Equations, representative of CN and HCN structures
- Physical and geomorphological interpretation of the scaling laws using a multifractal approach
- Novel criterion for channel heads detection based on variations in the multifractal signatures associated to the HCN and CN structures

Correspondence to:

P. Costabile,
pierfranco.costabile@unical.it

Citation:

Costabile, P., Costanzo, C., De Bartolo, S., Gangi, F., Macchione, F., & Tomasicchio, G. R. (2019). Hydraulic characterization of river networks based on flow patterns simulated by 2-D shallow water modeling: Scaling properties, multifractal interpretation, and perspectives for channel heads detection. *Water Resources Research*, 55, 7717–7752. <https://doi.org/10.1029/2018WR024083>

Received 21 SEP 2018

Accepted 14 AUG 2019

Accepted article online 19 AUG 2019

Published online 9 SEP 2019

Hydraulic Characterization of River Networks Based on Flow Patterns Simulated by 2-D Shallow Water Modeling: Scaling Properties, Multifractal Interpretation, and Perspectives for Channel Heads Detection

Pierfranco Costabile¹ , Carmelina Costanzo¹ , Samuele De Bartolo² , Fabiola Gangi¹ , Francesco Macchione¹ , and Giuseppe R. Tomasicchio² 

¹LAMPIT (Laboratorio di Modellistica numerica per la Protezione Idraulica del Territorio), Department of Environmental and Chemical Engineering, University of Calabria, Rende, Italy, ²Department of Engineering for Innovation, University of Salento, Lecce, Italy

Abstract This paper is focused on the contribution that the two-dimensional Shallow Water Equations could provide in respect to the fields of research devoted to the river networks analysis. The novelty introduced in this work is represented, in particular, by the hydraulic characterization of the river drainage networks, starting from flow patterns simulated by the two-dimensional Shallow Water Equations on high-resolution digital elevation model (DEM) through the analysis of water depths flowing down the hillslopes, channelized in both the main river and in all the tributaries or stored in small depressions. The first finding of this research is the determination of scaling laws that describe the relations between the water depth threshold, used to identify the network cells, and a dimensionless area, related to the total area of the network cells themselves. The observed bimodal scaling behavior has been considered as representative of the flow patterns belonging to the channel networks (CN) and hillslope plus channel networks (HCN), the physical and geomorphological interpretation of which has been provided from a multifractal point of view. In particular, the analysis of the multifractal spectra highlights significant variations in the multifractal signatures, between the CN and the HCN structures, leading to the proposal of a novel criterion for channels heads detection that has provided encouraging predictions of field observations.

1. Introduction

River networks represent the physical supports along which the volume of precipitation, transformed into surface runoff, is carried to the downstream part of a drainage catchment resulting, for the most severe event, in a flood wave. When the discharge hydrograph is generated mostly upstream from the area of study, runoff generation and routing processes are described essentially by a modeling chain in which the first model generates the runoff in subcatchments, resulting in a discharge wave that represents the upstream boundary condition for the second one (flood propagation model). However, when flooding events are combinations of an overflowing channel and overland flow, precipitation data should be imposed directly in the hydrodynamic model, simulating the runoff generation, leading to discharge and then to flooding. The general framework this paper belongs to is this second modeling approach.

In general, water flow on the surface can be simulated by solving mass and momentum balances, along the two planar directions, using gravity, pressure differences, and variations of local and convective inertia by means of the two-dimensional (2-D) depth-integrated shallow water equations (SWEs) model. The use of these equations in rainfall-runoff modeling has been limited in the past essentially for three reasons: stability problems of the numerical schemes used for the solution of the SWEs, prohibitive computational times required to run the numerical models, and the lack of high-resolution data which, therefore, did not completely justify the use of such complex modeling and, in particular, the presence of the inertial terms. Nowadays, no particular limitation seems to exist in the application of the 2-D SWEs for the simulation of surface runoff at a basin scale due to the development of more and more accurate numerical schemes, often running in parallel computing environments (e.g., Juez et al., 2016; Petaccia et al., 2016; Vacondio et al.,

2017; Wittmann et al., 2017), reducing dramatically the computational costs of the simulations. Moreover, the increasing availability of high-topographic detail offered by Light Detection and Ranging (LiDAR) surveys allows the use of fine meshes that, in turn, gives the opportunity for the resolution of small-scale flow patterns, increasing the relevance of inertial terms in the hydrodynamic simulation of the surface runoff (Cea & Bladé, 2015). Considering the added value that they can provide in terms of the physical representation of the overland flow phenomenon using high-resolution digital elevation model (DEM), the SWEs are increasingly recognized as the most suitable approach for the description of hydrodynamic-based surface runoff computations in rainfall-runoff simulations at the catchment scale (Bellos & Tsakiris, 2016; Bout & Jetten, 2018; Cavedes-Voullième et al., 2012; Cea & Bladé, 2015; Cea et al., 2010; Costabile et al., 2012, 2013; Fernández-Pato et al., 2016; Hou et al., 2018; Huang et al., 2015; Liang et al., 2015; Simons et al., 2014; Singh et al., 2015; Xia et al., 2017; Xia & Liang, 2018; Yeh et al., 2011).

It is important to observe here that all the efforts produced in the literature to analyze the predictive capability of the 2-D SWEs for surface runoff are mainly focused on the evaluations of the discharge hydrographs at some cross sections of a given basin. The flood hydrograph at the outlet of a basin is intrinsically linked to the dynamics of the surface runoff, flowing on hillslopes and channels networks, that in turn affects the shape, the arrival times, the rapidity that characterize the rising and falling limbs, and other parameters of the flood hydrograph itself. Therefore, river drainage networks can be studied from a hydrodynamic point of view, offering the development of novel tools of analysis and new insight into the research on that field.

In the literature, river networks have been studied from a physical, geometrical, and hydraulic point of view, introducing specific scaling laws that represent, within a given river basin, the relationships of scale invariance between topological variables (Dodds & Rothman, 1999; Gangodagamage et al., 2011; Hooshyar et al., 2017; Le & Kumar, 2014; Mantilla et al., 2012; Rodriguez-Iturbe & Rinaldo, 1997) or between channel characteristics such as mean depth, water surface width, mean velocity, length of active wet channels, and discharge (among the most recent studies, Dodov & Fofoula-Georgiou, 2004; Godsey & Kirchner, 2014; Hooshyar et al., 2015; Lawrence, 2007; Mersel et al., 2013; Nardi et al., 2006; Stewardson, 2005). In this research field, based on the contribution made by Mandelbrot (1982), several studies have applied fractal and multifractal analysis of river basins and networks in order to characterize many relevant geomorphologic and hydraulic-hydrologic variables (Ariza-Villaverde et al., 2013, 2015; De Bartolo et al., 2000, 2015, 2016; De Bartolo, Primavera, et al., 2006; Dodds & Rothman, 1999; Dombradi et al., 2007; Ijjasz-Vasquez et al., 1992; Perron et al., 2012; Rigon et al., 1993; Rinaldo et al., 1992, 1998; Saa et al., 2007; Veneziano & Iacobellis, 1999; Veneziano & Niemann, 2000), while in very recent years, they have been extended also into the context of urban drainage basins (Gires et al., 2017, 2018).

More generally, hydrological, but also geomorphic, analyses in a catchment require a differentiation between hillslopes and channels for the simulation of runoff generation and erosion mechanisms (Montgomery & Fofoula-Georgiou, 1993). In this field of research, several methods have been traditionally proposed to extract channel networks from DEM (see, e.g., Montgomery & Dietrich, 1988; O'Callaghan & Mark, 1984; Orlandini & Moretti, 2009; Orlandini et al., 2003, 2014; Tarboton, 1997; Tarboton et al., 1991), and further developments have been provided thanks to the modern LiDAR techniques (e.g., Hooshyar et al., 2016; Lashermes et al., 2007; Passalacqua et al., 2010, 2015; Pelletier, 2013; Pirotti & Tarolli, 2010; Tarolli & Dalla Fontana, 2009; Sangireddy et al., 2016; Shin & Paik, 2017).

The key issue that we are going to highlight in this work is how the SWEs could be nested in the research framework described so far. Specifically, we aim to shed new light on the research connected to the SWEs, exploring the novel potential contribution that the analysis of flow patterns, simulated by this kind of modeling, can provide to the analysis of aspects mainly devoted to the river basin drainage networks, such as the delineation of channel networks, the scaling laws, and the geometric properties of the river networks from a multifractal point of view. Therefore, the new knowledge that we can extract by the rigorous analysis of the different drainage structures, represented by flow patterns simulated by the 2-D SWEs, will be the focus and the core of this work.

Specifically, after a brief presentation of information and data related to the considered drainage basins (section 2), the methods used in this work, based on the 2-D SWEs for the determination of flow patterns identifying the river drainage networks and multifractal techniques for their theoretical interpretation, are presented and discussed (section 3). Section 4 is devoted to the analysis of the results, and it is divided into two parts: The first one concerns the characterization of flow patterns through specific scaling laws; the

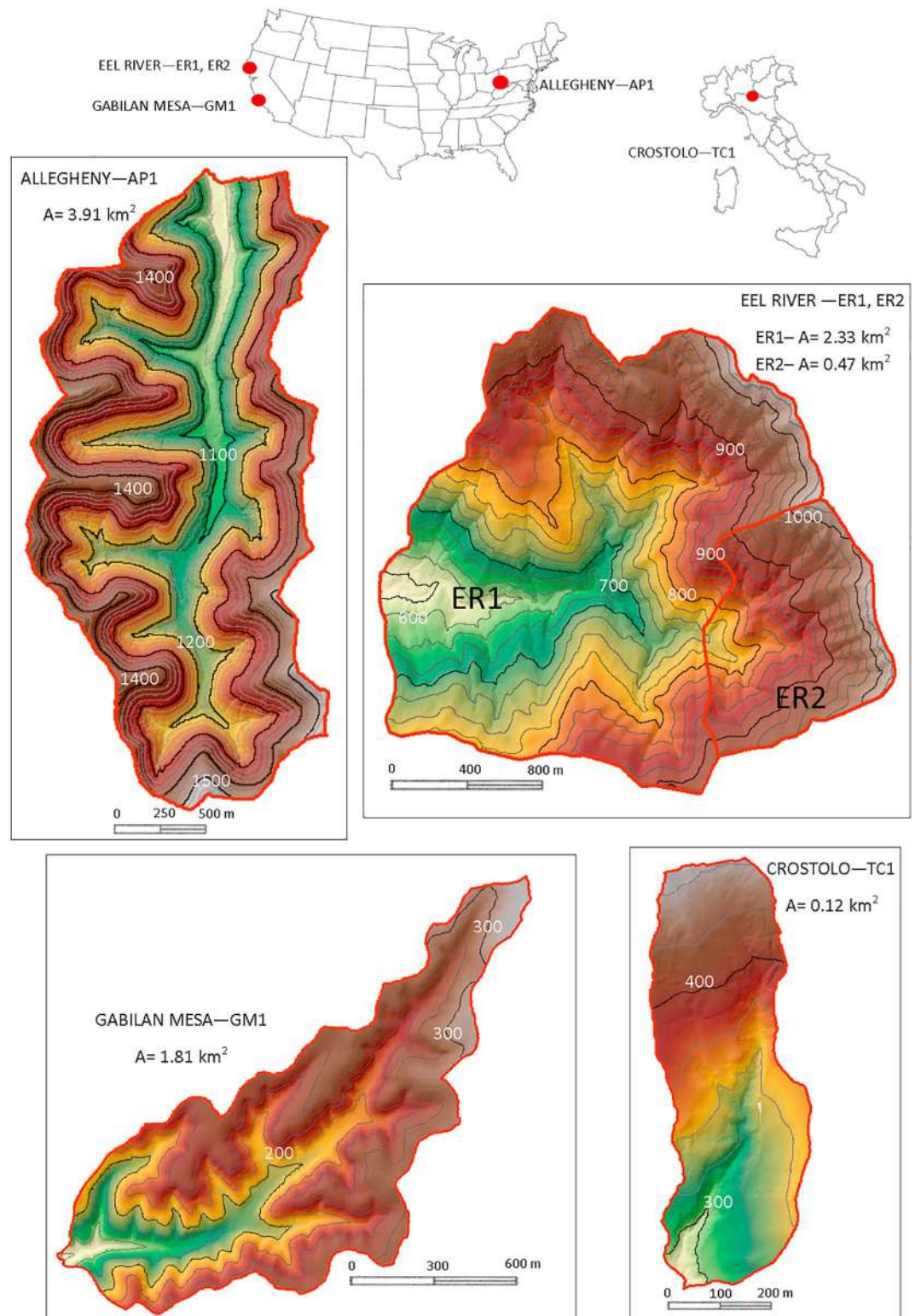


Figure 1. Representation and location of the river basins, analyzed in this study, for applications aimed at the hydraulic characterization of river networks by scaling laws.

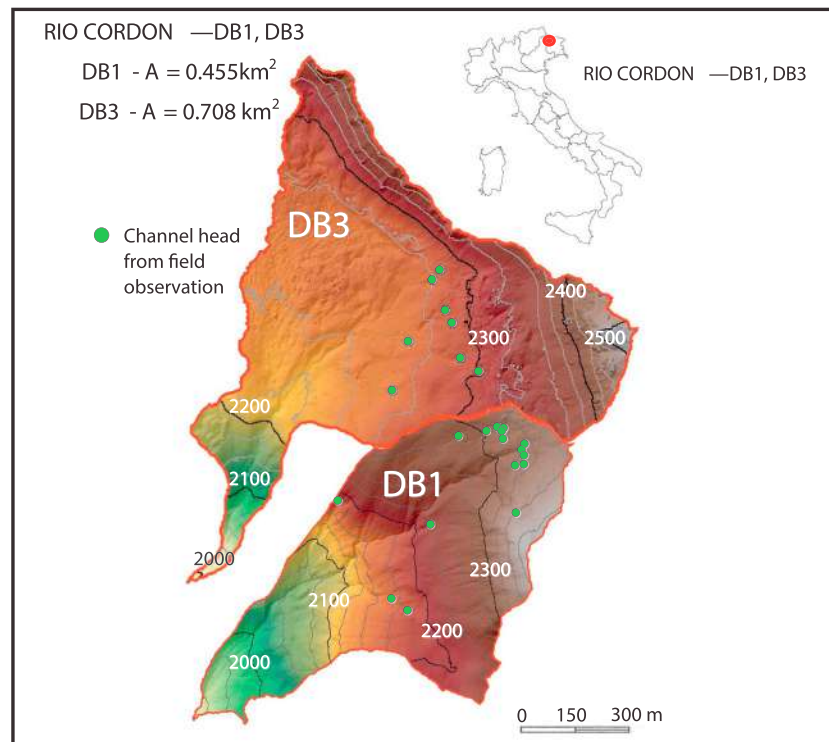


Figure 2. Representation and location of the river basins, analyzed in this study, for applications aimed at the detection of observed channel heads locations.

second one relates to their geometrical and morphological interpretation based on a multifractal approach. Finally, the contribution that these findings could give in terms of channel heads detection is presented and discussed (section 5) with reference to two basins for which field observations are available. The conclusions of the work are reported in section 6.

2. Study Areas

Five small drainage basins, namely, API, GM1, ER1, ER2, and TC1 (see Figure 1), have been used for the hydraulic characterization of river drainage networks, the scaling properties, and the multifractal analysis shown in section 4. Two basins, namely, DB1 and DB3 (see Figure 2), have been also used for the applications aimed at channel heads detection discussed in section 5.

All the information related to the considered basins are reported in Table 1.

Except for the case of ER1 and ER2, for which the data were downloaded from the internet (<http://www.opentopography.org/>), the DEMs were already available to the authors (De Bartolo et al., 2016). For each basin, LiDAR bare ground data were available and from which a 1-m DEM had already been extracted by the authors of the work cited above. In particular, the authors claimed that, at this fine resolution, “hillshades of the drainage basins were found to highlight clearly the morphology of channel and, specifically, the heads of these channels” (De Bartolo et al., 2016). For this reason, we can assume that the DEMs used here resolve the stream banks.

3. Methods

3.1. 2-D Fully Dynamic Shallow Water Model

The SWEs represent the basic physical principles related to mass and momentum conservation and can be written in conservative form as in equation (1):

$$\frac{\partial \mathbf{U}}{\partial t} + \frac{\partial \mathbf{F}}{\partial x} + \frac{\partial \mathbf{G}}{\partial y} = \mathbf{R} + \mathbf{S}, \quad (1)$$

Table 1
Information Related to the Basins Considered in This Paper

Basin name	Location	Area (km ²)	Mean slope (%)	Further information	Reference	Outlet location (latitude, longitude)
AP1	Allegheny Plateau region, Pennsylvania, USA	3.91	11	Smooth, soil-mantled slopes surround partially vegetated channels incised into colluvium	Perron et al. (2012); De Bartolo et al. (2016)	(39° 49' 36.60" N, 80° 24' 38.55" W)
GM1	Gabilan Mesa region, California, USA	1.81	6	Same as of AP1	Perron et al. (2012); De Bartolo et al. (2016)	(36° 36' 33.56" N, 121° 20' 33.32" W)
ER1	South Fork of the Eel River in Mendocino County, California, USA	2.33	18	The riverbed lies in a downcut channel with bedrock walls. It drains mountains areas characterized by narrow ridges and steep valleys	http://angelo.berkeley.edu/	(40° 36' 24.64" N, 124° 11' 54.28" W)
ER2	South Fork of the Eel River in Mendocino County California, USA	0.47	32	Same as of ER1	http://angelo.berkeley.edu/	(40° 36' 24.64" N, 124° 11' 54.28" W)
TC1	Italian Appennines	0.12	20	Both colluvial and alluvial channels are present, even though the channels of the first type are dominant	Perron et al. (2012); De Bartolo et al. (2016)	(44° 44' 50.31" N, 10° 35' 24.59" E)
DB3	Italian eastern Alps (the Dolomites)	0.702	42	Vegetation covers a substantial part of the surface of the two basins. The land is composed of sandstones with calcareous-marly rocky outcrops and deposits of scree and landslides and also landslide accumulations	Orlandini et al. (2011)	(46° 27' 51.90" N, 12° 6' 16.37" E)
DB1	Italian eastern Alps (the Dolomites)	0.455	49	Same as of DB3	Orlandini et al. (2011)	(46° 27' 51.90" N, 12° 6' 16.37" E)

where

$$\mathbf{U} = \begin{pmatrix} h \\ hu \\ hv \end{pmatrix}; \mathbf{F} = \begin{pmatrix} hu \\ hu^2 + gh^2/2 \\ huv \end{pmatrix}; \mathbf{G} = \begin{pmatrix} hv \\ huv \\ hv^2 + gh^2/2 \end{pmatrix}; \mathbf{R} = \begin{pmatrix} r - f \\ 0 \\ 0 \end{pmatrix}; \mathbf{S} = \begin{pmatrix} 0 \\ gh(S_{0x} - S_{fx}) \\ gh(S_{0y} - S_{fy}) \end{pmatrix}, \quad (2)$$

where t is time, x and y are the horizontal coordinates, h is the water depth, u and v are the depth-averaged flow velocities in x - and y - directions, r is the rain intensity, f is the infiltration losses, g is the gravitational acceleration, S_{0x} and S_{0y} are the bed slopes in x - and y - directions, and S_{fx} and S_{fy} are the friction slopes in x - and y - directions that can be calculated from Strickler's formula.

The SWEs are sometimes referred to by the term “fully dynamic” approach, in order to separate them from their approximations, the so-called kinematic and diffusive wave models. In particular, the kinematic flow approximation, which simplifies water flow by ignoring pressure and inertial momentum, gained popularity in the early years of numerical modeling for its computationally efficient and robust estimations of flow patterns (Stephenson & Meadows, 1986). The diffusive flow approximation implements pressure in the momentum equations (see, among the first ones, Di Giammarco et al., 1996; Tayfur et al., 1993).

Several studies in the literature have shown several drawbacks and limitations in the use of simplified models. For example, Costabile et al. (2012) have shown that the models performances are similar in very simplified tests where the topography is reduced to a flat surface, while, in more complex situations, poor predictions of experimental data have been provided by the simplified models. Starting from the analysis of the water depth profile, in a situation characterized by mixed subcritical-supercritical flow, Yeh et al. (2011) suggested the use of the fully dynamic modeling in order to avoid important distortions of the physical process as simulated by simplified models. More recently, Bout and Jetten (2018) have found important differences in terms of simulated spatial patterns of overland flow and, therefore, in the connectivity and concentration of flow. In particular, the authors highlighted that, compared to the dynamic flow which performed best, kinematic and diffusive flows, respectively, overestimate and underestimate flow concentration due to the inherent properties of the simplified models.

Other studies confirmed the fact that the diffusive wave model is less accurate and less stable than the dynamic wave model, pointing out the relevance of inertial terms, at least in rainfall-runoff modeling and flood propagation in urban areas (Cea et al., 2010; Costabile et al., 2017; Schubert et al., 2008). Therefore, the drawbacks associated with the use of simplified models, highlighted in these studies, suggest the use of SWEs for reliable simulations of surface runoff, such as those presented in this work.

3.1.1. Numerical Issues and Computational Domains

Except in some theoretical cases, it is not possible to derive analytical solutions for the 2-D SWEs, and therefore, numerical schemes have to be used in order to obtain a solution for these equations. In particular, on the basis of the authors' experience on these kind of simulations (Costabile & Macchione, 2015; Costabile et al., 2012, 2013, 2017; Macchione, Costabile, Costanzo, & De Santis 2019; Macchione, Costabile, Costanzo, & De Lorenzo, 2019), the first-order shock-capturing scheme reported in Appendix A has been used here. It is important to observe that this numerical model used here is characterized by well-balanced properties. Therefore, it is possible to use DEM data without removing topographic depressions, as performed in the use of traditional methods for the automatic extraction of river networks.

The computational domain has been composed of triangular cells, having the same area as the DEM resolution (1 m^2). Since there is no need to use a more refined grid in areas characterized by significant topographic variations, as usually performed in flood mapping studies on large domains (see Costabile & Macchione, 2015), the elements of the computational grid used in all the simulations have the same size throughout the basin. In particular, the nodal generation process was carried out using Surface-water Modeling System-Aquaveo™. This software has a mesh generator system, in a Geographic Information System environment, able to create computational grids according to different algorithms. In order to take into account the effects of the computational domain on the results that will be presented in the next section, we have used two different approaches to obtain two alternative triangular grids (see Figure 3). The first one, namely, G-1, is based on the so-called “paving method” that uses an advancing front technique to fill the polygon with elements. In particular, based on the vertex distribution on the boundaries, equilateral triangles are created on the interior to define a smaller interior polygon. Specifically, starting from the polygon delimiting the basin (Figures 3a and 3b), we have specified the distance L_T , between two consecutive

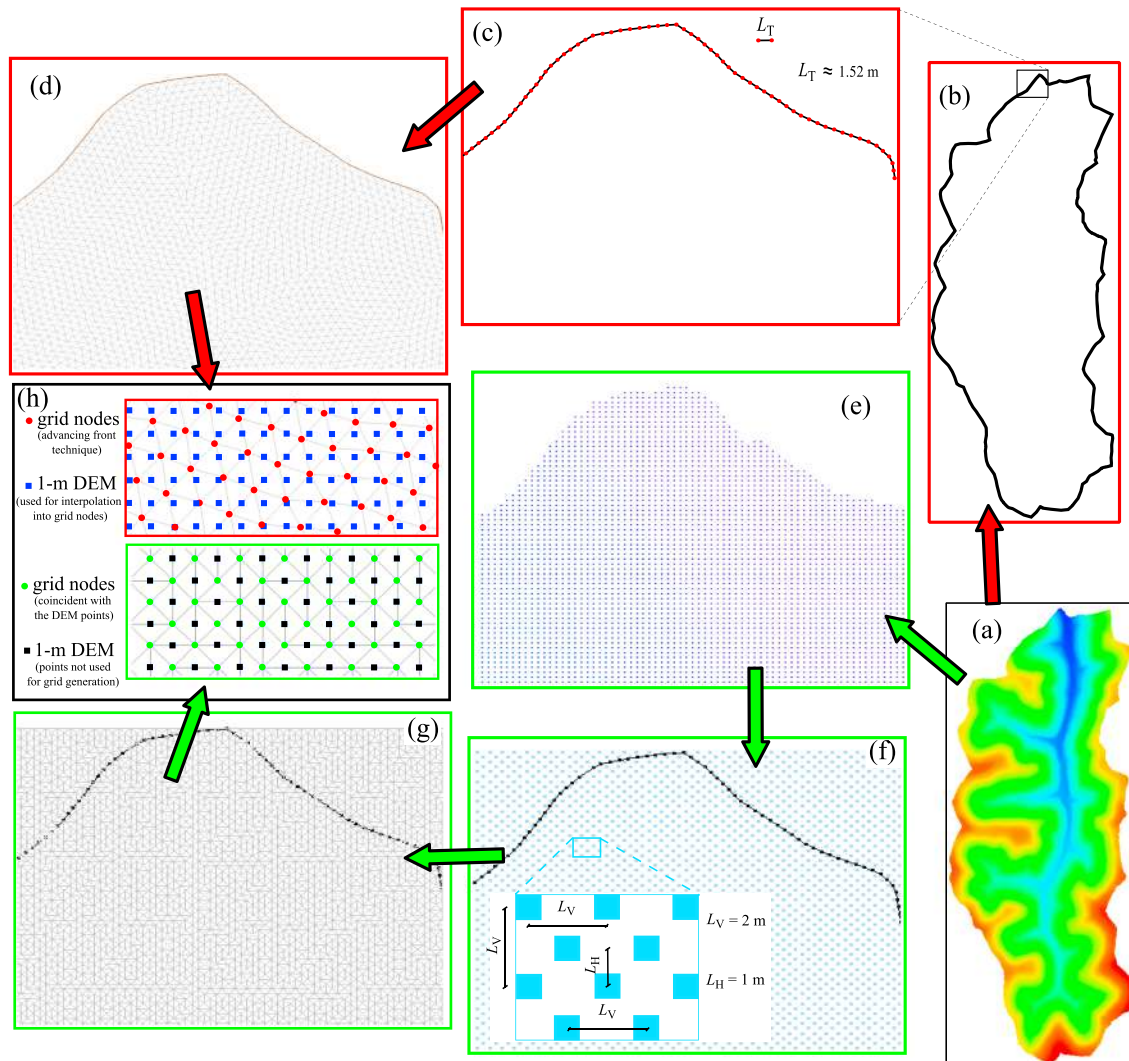


Figure 3. Grid generation processes starting from DEM points (a): (b–d) G-1 grid, (e–g) G-2 grid, and (h) their comparison. DEM = digital elevation model.

nodal points along that boundary, in order to generate equilateral triangular elements having an area equal to 1 m^2 . Therefore, L_T should be approximately equal to 1.52 m (Figure 3c). Then the grid generation process is automatic (Figure 3d), according to the paving method, and the final computational domain can be obtained by interpolating the original 1-m DEM into the grid nodes (see, respectively, blue squares and red circles in Figure 3h). Therefore, according to this technique, the grid points do not generally coincide with the location of 1-m DEM points. On the contrary, the second approach generates the computational grid in the same locations as the original 1-m DEM points. However, it is evident that the connection of the DEM points leads to the generation of triangular elements that have an area equal to 0.5 m^2 , which is equal to half of the area considered before. Therefore, we have removed some points of the original DEM (shown in Figure 3e), according to the scheme presented in Figure 3f. In practice, we have removed one point every two points in the horizontal direction, following a staggered configuration. Then we have connected these points, generating the grid shown in Figure 3g (called G-2 hereafter). This idea is further represented in Figure 3h, in which the original DEM points used for the triangular grid generation are depicted using green circles while the remaining ones are highlighted using black squares.

The G-2 grid has been used only to check the effects of the grid generation process on the results. Therefore, except for this purpose, all the results presented in section 4 have been obtained using the G-1 grid. To give a rough idea of the G-1 grid, some details related to the AP1 basin are shown in Figure 4. This figure represents

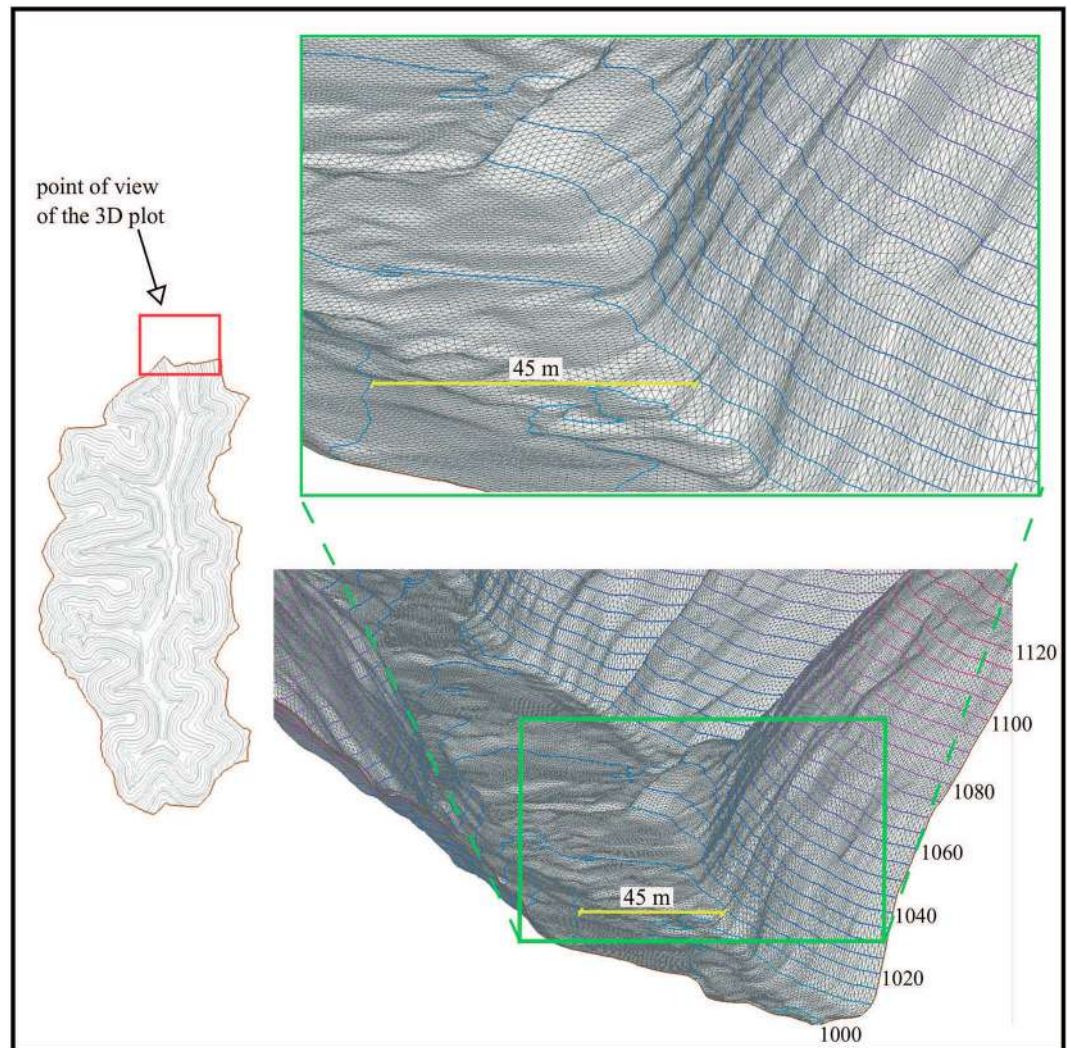


Figure 4. Downstream view of the computational grid at the outlet of the AP1 basin. 3-D plot with view point up to the main channel.

a 3-D plot of a downstream view of the basin outlet (the viewpoint for this figure is looking up to the main channel).

It might be important to underline here that, to the authors' knowledge, no application of the 2-D SWEs modeling at a basin scale has been performed using DEM resolution up to 1 m^2 , since the grid size element commonly used in the literature is significantly greater than that used here (see, e.g., Bellos & Tsakiris, 2016; Fernández-Pato et al., 2016; Nguyen et al., 2016; Xia et al., 2017).

3.1.2. Use of the SWEs for the River Networks Analysis and Modeling Assumptions

The first problem that should be faced is the identification of the flow patterns representing river drainage networks. This has been resolved starting from the numerical solution of the SWEs that, once a specific precipitation input has been assigned, gives the spatial and temporal evolution of the water depths h , within the basin, in addition to the velocities u and v . These hydrodynamic variables are computed in the centroid of the triangular cells that characterize the computational domain (see Figure A1). The approach followed here considered a heavy rainfall, constant in time and uniform in space. Two main assumptions have been introduced in the computations presented in this work. The first one regards the runoff generation mechanism. The modeling approach used here commonly ignores the interaction with groundwater, because it is mainly devoted to the simulation of extreme rainfall events in which infiltration excess is considered to be the dominant process in the surface runoff production. Therefore, the use of a specific model for the computation of the infiltration losses f is necessary to obtain the consequent net rainfall $s = (r - f)$. However,

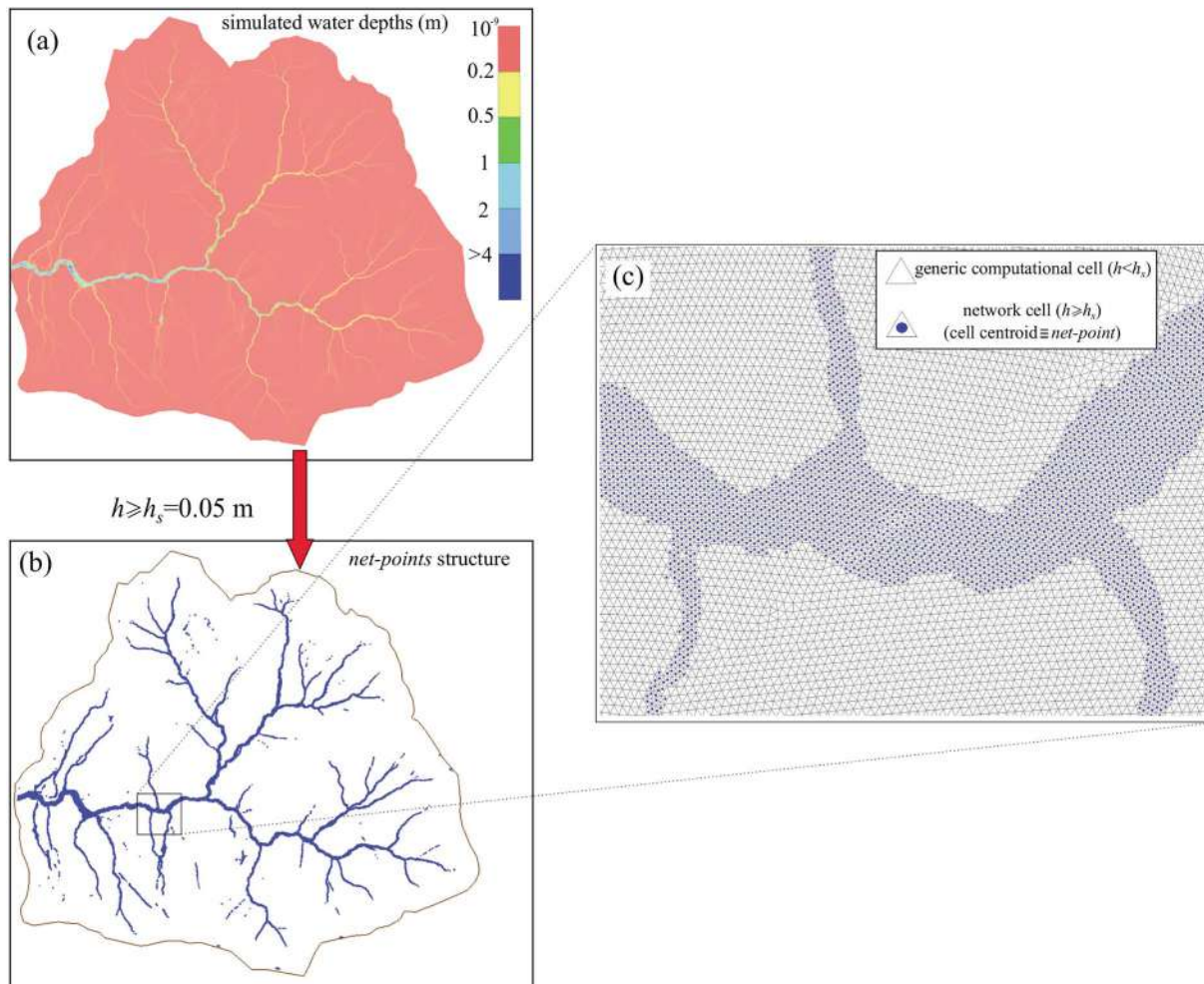


Figure 5. *Net – points* generation process. Water depths map simulated by the 2-D shallow water equations for the ER1 basin (a), cells centroid for which the computed water depths values are equal to or greater than a selected threshold value h_s (b), and details of *net – points* structures represented by blue circles (c).

for the purpose of this work, the SWEs model has been initialized using a fictitious inflow s to route everywhere into the basin, according to the mass and momentum balances, in order to detect the path through which the water is collected in the channels, stored in small depressions, or flows down the hillslope.

A second assumption concerns the roughness values used for the computation of friction slopes, for which a similar reasoning can be applied. The roughness values to assign to each cell of the computational domain should be estimated carefully and differentiated throughout the basin according to land use and soil type (see, e.g., Costabile et al., 2013). Moreover, roughness values for shallow flows on hillslopes, in which the depth is much less than the size of the roughness elements, are expected to be much larger than those in channels. However, keeping in mind the objectives of this work, no differentiation has been introduced for the Strickler coefficient value. Nevertheless, both the assumptions described above will be discussed later on in the paper (see section 4.1.1) in order to assess their influences on the scaling properties presented in section 4.1.

The rain duration assumed in the simulations has been considered as infinite. This choice aims at the evaluation of the hydraulic response of the basin in the most critical situation, in which the specific discharge (discharge per unit of area) at the outlet section reaches its maximum value, given by the net-rainfall intensity considered as input. In other words, the hydraulic situations analyzed here refer to steady-state conditions.

Once the spatial distribution of the water depths $h(x, y)$ in the basin is known, in a given instant of time subsequent to the stabilization of the discharge at the outlet section (see Figure 5a), it is possible to obtain

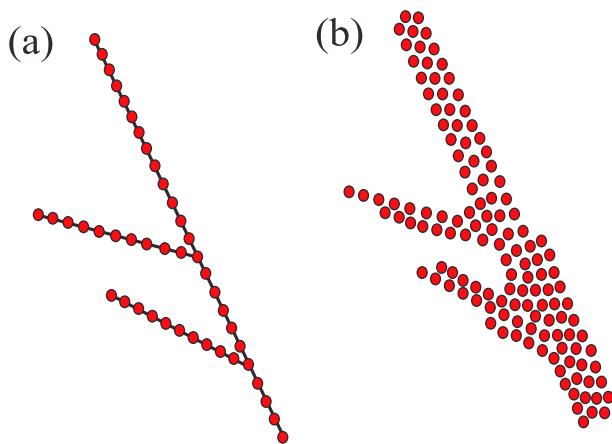


Figure 6. Tree-like fluvial schemes: skeleton composed of a set of lines, with no width, following the linear properties of the quantitative fluvial geomorphology (a) and set of *net - points* derived from the shallow water equations model based on a 2-D discretization of the river network geometry (b).

an infinite number of river networks structures. This is due to the specific water depth value identified as threshold beyond which a particular cell is considered as belonging to the river network itself (see Figure 5b). Therefore, the generic flow pattern representing the river network can be obtained as a set of points, the coordinates of which are determined by the centroid of those cells having a water depth, in a steady-state situation, equal to or greater than the selected threshold value. In what follows, a cell assigned to the river network will be called “network cell” (see Figure 5c). The term *net - points* will be used to denote the set of points that defines the river drainage network. Therefore, in the context of the multifractal analysis presented in section 3.2, the *net - points* are coincident with the coordinates of the centroid of the network cells.

It is important to observe here that a comparison between the 2-D SWEs approach and the traditional techniques for automatic channel network extraction from DEM is not so immediate, and probably, it might not be very meaningful. In fact, the automatic channel network extraction from DEM have been specifically developed to fully exploit the analysis in a GIS environment and therefore should be easy to implement and very efficient from a computational point of view. In this respect, considering a complex numerical simulation, typical of the 2-D SWEs, as a method for

channel network extraction might be inappropriate. However, it should be observed that a major assumption of the methods for the automatic extraction of river networks is that flow is driven only by gravity, and therefore, flowpaths are only the consequences of the morphology of the basin. From a hydraulic point of view, this means steady and uniform flow (Shelef & Hilley, 2013) that, within the context of the physically based modeling of the surface runoff, implies a kinematic modeling. Therefore, the traditional approach might potentially suffer from all the drawbacks highlighted in section 3.1. Furthermore, as underlined by Limaye (2017), the assumption of flow driven only by gravity cannot capture locally divergent flow paths in which the relationship between flow and topography is more complex.

3.2. General Features of the Multifractal Measures of River Networks

While fractal analyses aim at the determination of a fractal dimension, which quantifies the ability of the network to fill a plane, multifractal measures require a sequence of generalized fractal dimensions or multifractal spectra, describing the geometric complexity of dense and sparse clusters of the drainage networks (see, e.g., De Bartolo, Veltri, et al., 2006; Feder, 1988; Rodriguez-Iturbe & Rinaldo, 1997).

In general, the term “multifractal measure” is referred to the distribution of a specific physical quantity over a support, geometrically represented by a plane, a volume, or a fractal itself (Feder, 1988). This kind of analysis was first applied to the river network by Ijjasz-Vasquez et al. (1992) and Rinaldo et al. (1992). Then, multifractal analysis in the literature mainly refers to other important variables such as catchment areas, slopes Rodriguez-Iturbe et al. (1994), topography (Veneziano & Iacobellis, 1999; Veneziano & Niemann, 2000), network optimization (Rigon et al., 1993; Rinaldo et al., 1998), dissipation energy (Ijjasz-Vasquez et al., 1993; Rinaldo et al., 1991), channel initiation function, and the width function (Rodriguez-Iturbe & Rinaldo, 1997).

Besides these traditional approaches, the multifractal measures have been characterized by considering the distribution of points defining the geometry of a generic set on a fractal or multifractal support (see, e.g., Harte, 2001; Olsen, 1995). Following these ideas, De Bartolo et al. (2000) and De Bartolo, Primavera, et al. (2006) applied multifractal techniques to analyze the geometry of the river networks. These studies demonstrated that the characterization of fluvial structures by *net - points* and specifically their measure (see next section) can be considered as a fluvial geomorphological magnitude like the other ones mentioned previously.

In all the studies cited above, the support of measures of river networks is represented by a collection of *net - points* discretized according to a tree-like fluvial scheme. Except for some works related to the application of the so-called fat fractal formalism that does consider the channel width (Karlinger & Troutman, 1992; Karlinger et al., 1994), the tree-like fluvial scheme is traditionally characterized by a skeleton composed of a set of lines, following the linear properties of the quantitative fluvial geomorphology (Strahler, 1975; see

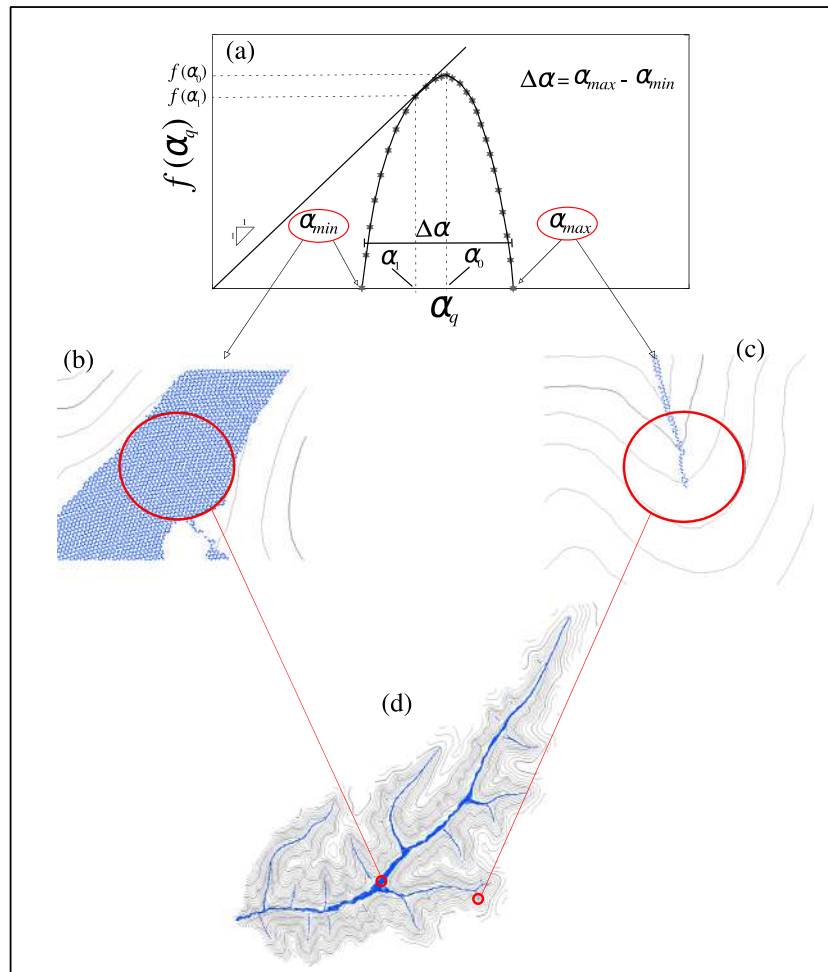


Figure 7. Practical meaning of the multifractal spectrum: relevant quantities (a) and connection with geomorphological features of the river networks (b–d).

Figure 6a). The proposed approach used here is different from the traditional ones because it generalizes the support of measures, introducing a tree-like fluvial structure composed of a collection of points discretizing the 2-D geometry of the structure itself. For this reason, the characterization of river *net – points* performed here is a point of novelty not only because it has been obtained using a hydrodynamic model but also especially because it is based on a 2-D discretization of the river basin geometry, which implicitly describes the drainage network width in a high-resolution scale closer to reality (see Figure 6b).

3.2.1. Multifractal Spectra: Meaning and Significant Quantities for the Analysis of 2-D SWEs

Set of Points

The *net – points* representing the river network (see, e.g., Figure 5) are the geometric support where it is possible to perform a covering measure. This means covering the set of *net – points* using N_c nonoverlapping cells, the side size of which is equal to ϵ_i , $1 \leq i \leq N_c$ and, then, to define the measure (or probability or mass) in the i th box of the partition as the ratio, p_i , between N_i and N_t , that are, respectively, the number of points falling in the i th cell and the total number of points. The measure is expressed as a power law relating the mass p_i to the cell size of ϵ_i through a singularity exponent, known also as the Lipschitz-Hölder exponent (please refer to Appendix B for all details related to the multifractalism formalism used in this work).

When the measures show a multifractal behavior, the spectra assume an inverted U-shape, characterized by a maximum value that is the fractal dimension of the river network support $f(\alpha_0)$ corresponding to the singularity dimension α_0 (see Figure 7a), and a negative concavity on the range of values $[\alpha_{min}, \alpha_{max}]$. In particular, Beck (1990) and Beck and Schlögl (1993) have shown that the maximum mass, $p_{max} = \max_i p_i$, and the minimum mass, $p_{min} = \min_i p_i$, are associated with the minimum and maximum scaling indices

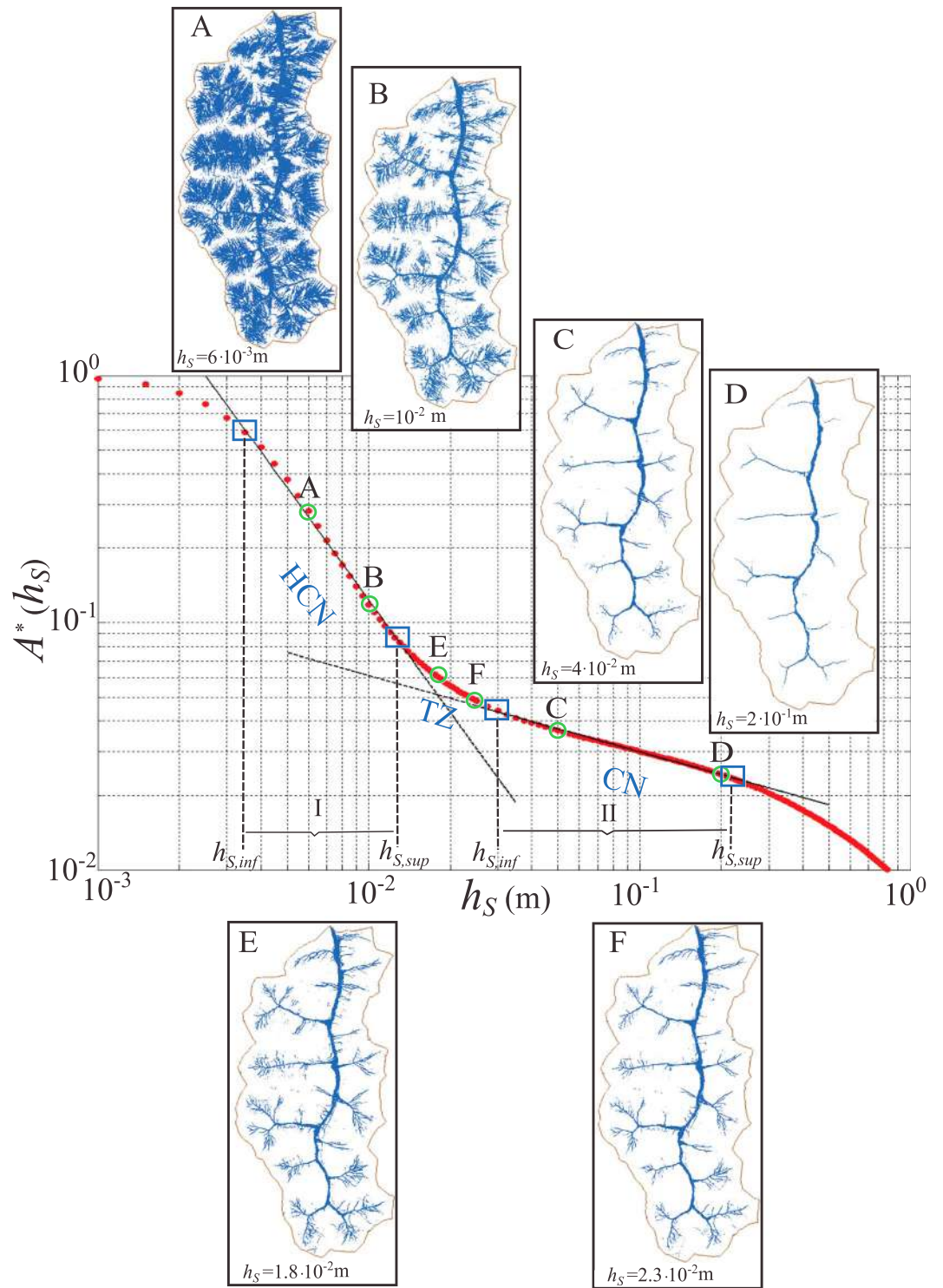


Figure 8. Bimodal behavior of the dimensionless river network area A^* against the water depth threshold h_s used to identify the network itself. Representation of the river networks associated to specific values of h_s (A–F) for the AP1 basin.

Table 2
Scaling Results of the Analyzed River Networks

Basin Name	Net-points structure	$h_{s,inf}$ (m)	$h_{s,sup}$ (m)	b
AP1	HCN	0.004	0.013	1.610
	CN	0.030	0.210	0.300
ER1	HCN	0.030	0.013	1.390
	CN	0.020	0.300	0.640
GM1	HCN	0.003	0.011	1.710
	CN	0.017	0.210	0.450
ER2	HCN	0.003	0.010	1.460
	CN	0.011	0.110	0.840
TC1	HCN	0.003	0.011	1.370
	CN	0.012	0.110	0.700

Note. HCN = hillslope plus channel networks; CN = channel networks.

α_{min} and α_{max} , respectively, through the couple of equations (3)

$$p_{max} = \epsilon^{\alpha_{min}}, \quad p_{min} = \epsilon^{\alpha_{max}}. \quad (3)$$

These relations define the level of rarefaction or aggregation of the *net – points* characterizing the river drainage structures. In particular, recalling that in the box counting approach $\epsilon \rightarrow 0$, relations (3) highlight that, for a fixed value of ϵ , the greater α_{min} (α_{max}) the smaller p_{max} (p_{min}). From a practical point of view, since p_{max} (p_{min}) represents the ratio between the maximum (minimum) number of points in a covering box and the total number of points, it is clear that α_{min} (α_{max}) is a quantity strictly connected with the areas of maximum (minimum) density of *net – points*. This means that α_{min} is representative of the flow channelized in the main river and tributaries, in which a high level of aggregation occur, while α_{max} is representative of peripheral parts of the river network in which the rarefaction of the *net – points* is greater than in other parts of the network itself. This concept is graphically represented considering two details (Figures 7b and 7c) of a typical output of the 2-D SWEs shown in Figure 7d. Moreover, in Figure 7a, the so-called spectrum width ($\Delta\alpha = \alpha_{max} - \alpha_{min}$) has been highlighted. This is another relevant quantity of the spectrum that provides practical indications related to the multifractal character of the river networks, which increases as $\Delta\alpha$ increases too. The river structures are more intricate and heterogeneous as the value of $\Delta\alpha$ increases. Therefore, the analysis of $\Delta\alpha$ values can provide fundamental information related to the analysis of branching structures in river networks. Finally, another two particular quantities of the multifractal spectrum, mentioned later on in the paper, are the dimension of entropy $f(\alpha_1)$, where the greater part of the *net – points* is concentrated, and the correlation dimension $f(\alpha_2)$, connected to the probability that two random points fall together into the same covering box, or a cell, of a given size. It is also possible to define $f(\alpha_1)$, graphically, by the intersection of the 1:1 line with the $f(\alpha)$ spectrum (see Figure 7a). For further explanations of these quantities, one can refer to Rodriguez-Iturbe and Rinaldo (1997).

It is essential to underline that the approach used here belongs to the so-called Direct Scaling Analysis, in which the focus is on the singularity exponents α and in particular on α_{min} and α_{max} because they are related to the most significant parts of the physical measures represented by the probabilities p_i (equation (3)). Therefore, these measures are much more significant than the fractal dimensions $f(\alpha)$ because the latter ones, though important when connected to a theoretical model of a river network, do not have a practical use for the channelization process.

4. Results and Discussion

4.1. Scaling Analysis of River Networks Derived From 2-D Shallow Water Model

In order to analyze the flow patterns simulated by the shallow water modeling, as a function of h_s , we introduce the variable A^* . It represents a dimensionless area defined as the ratio between the total area of the network cells, A_t , that is the sum of the areas, $A(j)$, of those cells j having a water depth $h(j)$ equal to or greater than h_s itself, and the total basin area, A :

$$A^*(h_s) = \frac{A_t}{A} = \frac{\sum_j A(j)}{A}, \quad j \in I_{NC}(h_s), \quad (4)$$

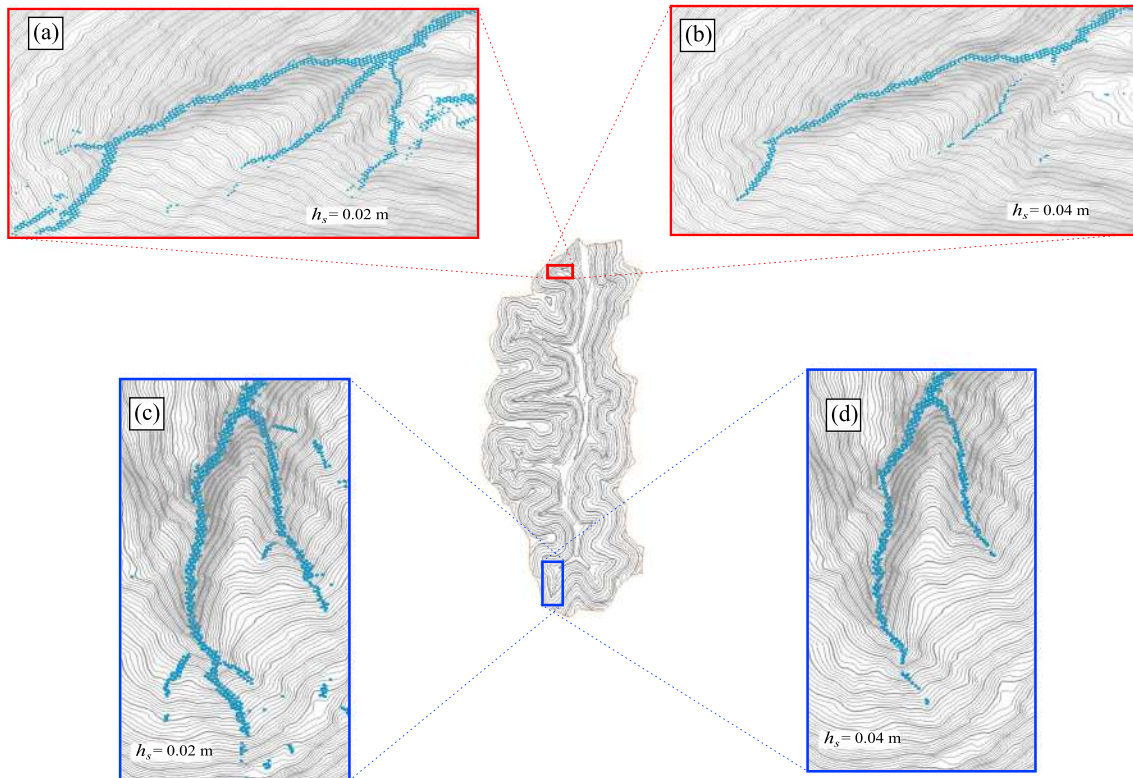


Figure 9. AP1 drainage basin: details of *net – points* structures belonging to transition zone (a, c) and channel network (b, d) in relation with the digital elevation model contour levels (every 1 m).

where $I_{NC}(h_s)$ is the set of network cells for a given value of h_s . The main aspect of the $A^* - h_s$ relation is that the points of coordinates $(\log h_s, \log A^*)$ tend to be arranged according to two linear laws having significantly different slopes, as highlighted by the Segments A–B and C–D represented in Figure 8. Moreover, *net – points* representing the simulated river drainage structures are more and more concentrated in the main channels as the value of h_s increases, while, on the contrary, as the value of h_s decreases, more and more points fall also on the hillslopes (Figure 8, A–D). Clearly, for the lower values of h_s , the points tend to cover the whole basin. On the other hand, the rapid increase of A^* , with the decrease of h_s , detected by the slope of the Segment A–B, is a strong indication of the fact that larger and larger areas of the basin are being selected, involving progressively all the hillslopes, reaching, practically, the whole basin. These considerations, although they cannot be intended as theoretical justifications, induce us to argue that two different scaling laws might be representative of two different river drainage structures: hillslope plus channel networks (HCN) and channel networks. The analytical characterization of the behavior observed in Figure 8 can be performed by introducing two different power laws, obtained by a numerical procedure aimed at maximizing the coefficient of determination R^2 within the ranges $[h_{s,inf}, h_{s,sup}]_I$ and $[h_{s,inf}, h_{s,sup}]_{II}$ that define also the cutoff limits beyond which the measure diverges. In particular, the points characterized by h_s being lower than $h_{s,inf}$, in the first scaling range, identify the plane-filling behavior of the river network, which is the tendency, shown by the river drainage structure, to cover the whole drainage basin. On the contrary, the points having h_s greater than $h_{s,sup}$, related to the second scaling range, can be interpreted as representative of structures with a poor development of the channel network.

The analytical law describing the scaling properties for both HCN and CN can be written as in the following formula:

$$A^* = ah_s^{-b}, \quad (5)$$

in which $a [L^b]$ and $b [-]$ are two parameters. b is the scale parameter. The numerical values of the scaling ranges and the parameter b , for each basin analyzed in this paper, are reported in Table 2. The coefficient of determination, for all the scaling ranges, is greater than 0.99.

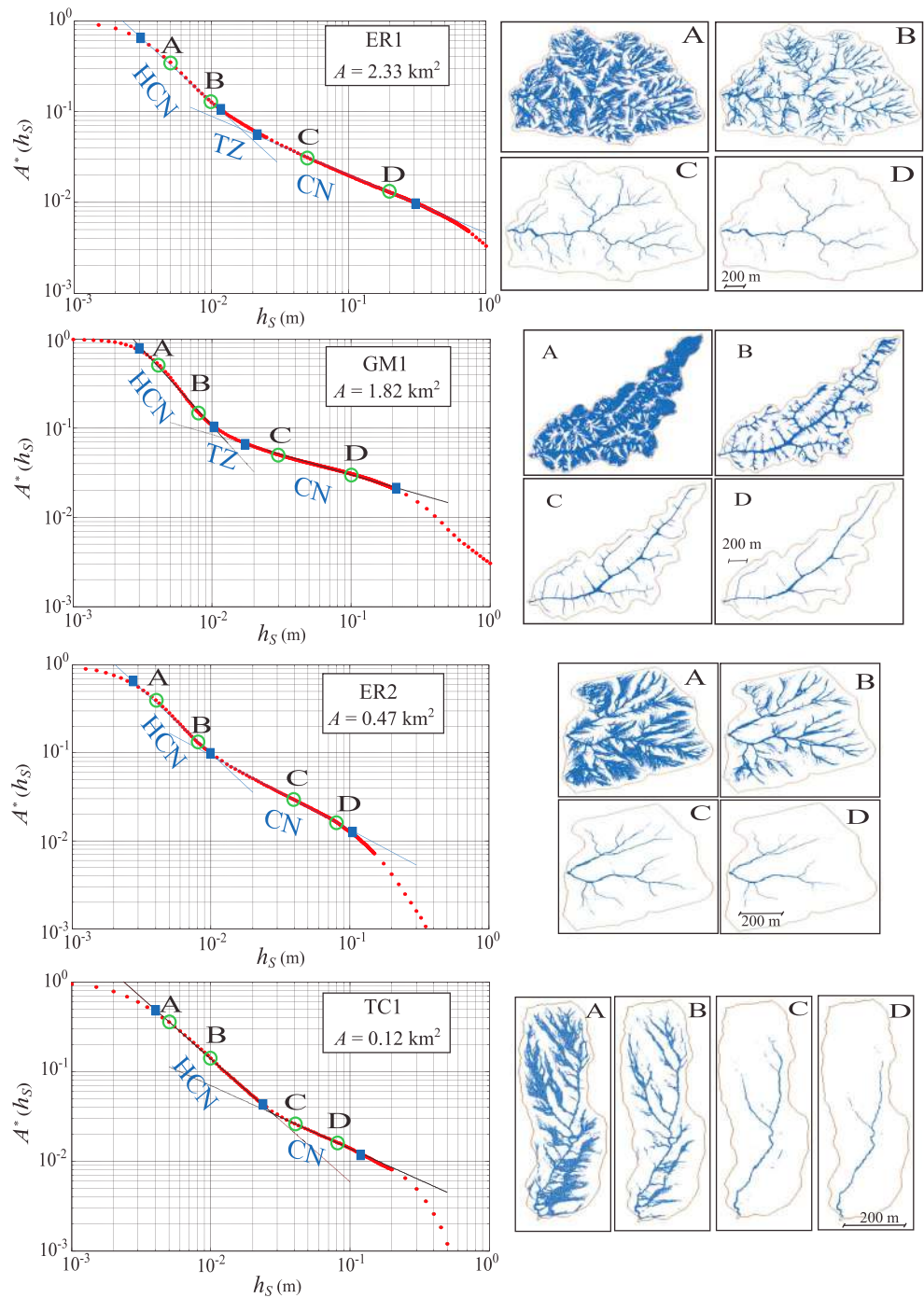


Figure 10. $A^* - h_s$ curve for the ER1, GM1, ER2, and TC1 river. HCN = hillslope plus channel networks; TZ = transition zone; CN = channel networks. basins.

The two scaling ranges allow also the identification of a particular area of the figure in which the points deviate from the bimodal behavior determined by the scaling laws relative to the HCN and CN configurations. This area represents a transition zone (TZ) characterized by a gradual shift from the HCN to CN structures. As an example, in Figure 8E and 8F, two river structures belonging to TZ are shown.

In order to better discuss the *net - points* structures belonging to both TZ and the beginning of CN, we have provided two details in Figure 9. In this figure, we have represented the contour lines of the basin, every 1 m, in order to detect the morphology of the channels. Figures 9a and 9b refer to the situation located near

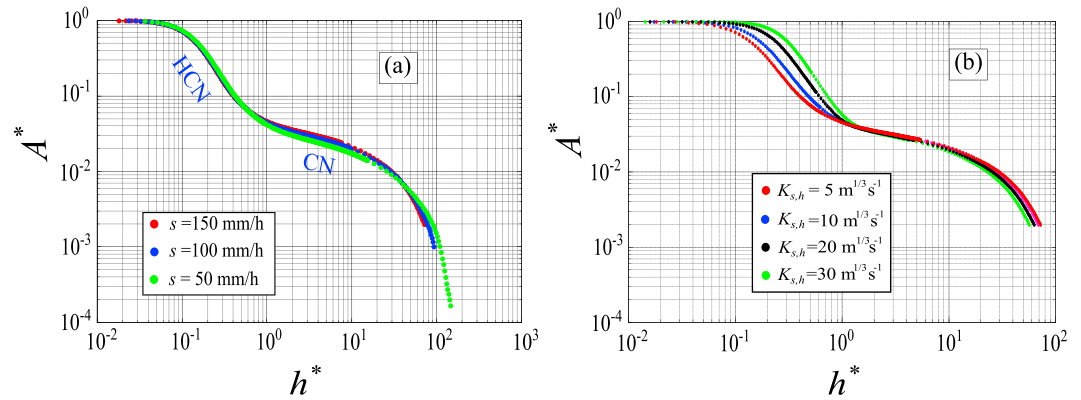


Figure 11. AP1 drainage basin: influence of the fictitious inflow s (a) and hillslope Strickler coefficient (b) on $A^* - h^*$ curve ($h^* = h_s/h_m$, in which h_m is the mean value of the water depths computed throughout the basin). HCN = hillslope plus channel networks; CN = channel networks.

the outlet of the basin (see red rectangle), while Figures 9c and 9d represent the *net - points* structures in an upstream area (see blue rectangle). Both the structures show the tendency to cover the stream channels. It is not very simple to say which is the best configuration in relation to the channel heads position because their exact location is quite hard to identify without going into the field. Nevertheless, the TZ structure ($h_s = 0.02$ m) is more heterogeneous than the CN one ($h_s = 0.04$ m), detecting also areas characterized by small depressions.

The bimodal behavior of the dimensionless area, related to the network cells, observed for AP1 can be detected in all the analyzed basins (see Figure 10), but the scaling exponents b and scaling intervals are different (see Table 2). As regards the HCN configurations, the values of the scaling exponents fall in a relatively narrow range, about 1.4–1.7, with a maximum difference up to 20%. The differences among the CN structures are much more important since the scale exponents range between 0.3 and 0.8. This fact could be explained by the significant differences existing among the considered basins in terms of the drainage patterns and the valley structures. In any case, the analysis of the reasons that induce the different values of the scale exponents goes beyond the purpose of this work, even though some considerations will be provided in the multifractal analysis of the results.

Finally, it should be observed that, being a scaling relation between hydraulic and geometric variables of the basin, the scaling law presented has some points of contact with the so-called “hydraulic geometry” concept, introduced formally by Leopold and Muddock (1953) and extensively improved and further analyzed in several studies in the last decades (Barber & Gleason, 2018; Gleason & Wang, 2015; Sofia et al., 2015; Xia et al., 2017). It is necessary to underline that the abovementioned studies concern essentially “at-a-station” hydraulics, which means the estimation of 1-D variables related to a given cross section (water depth, width of the section, mean velocity, and discharge). Contrarily, the experimental scaling properties presented here could be intended as “2-D” information throughout the basin since they refer to the water depths and to the relative cumulative areas, computed in the centroid of cells composing a 2-D computational domain. In this sense, though not explicitly linked to discharge values, our results could contribute to support the new approach proposed by Gonzalez and Pasternack (2015), termed “hydraulic topography,” which relies on 2-D hydrodynamic simulations and high detailed topographic data for analyzing discharge-dependent hydraulics.

4.1.1. Influence of the Fictitious Net Rainfall, Roughness Values, and Computational Grids on the Proposed Scaling

The first issue concerns the values of the fictitious net inflow (s) assumed in the calculations and how much this value affects the scale parameter b . For this reason, three simulations have been performed using different values of s (50, 100, and 150 mm/hr). Since a variation of the rainfall intensity provokes a different hydraulic response within the basin, the variable h^* , defined as the ratio between h_s and the mean value of the water depths computed throughout the basin at the end of the simulation (steady-state condition), is introduced here in order to compare the different values of the water depths within the basin related to different inflows s . The behavior of A^* as a function of h^* is represented in Figure 11a. Despite the fact that

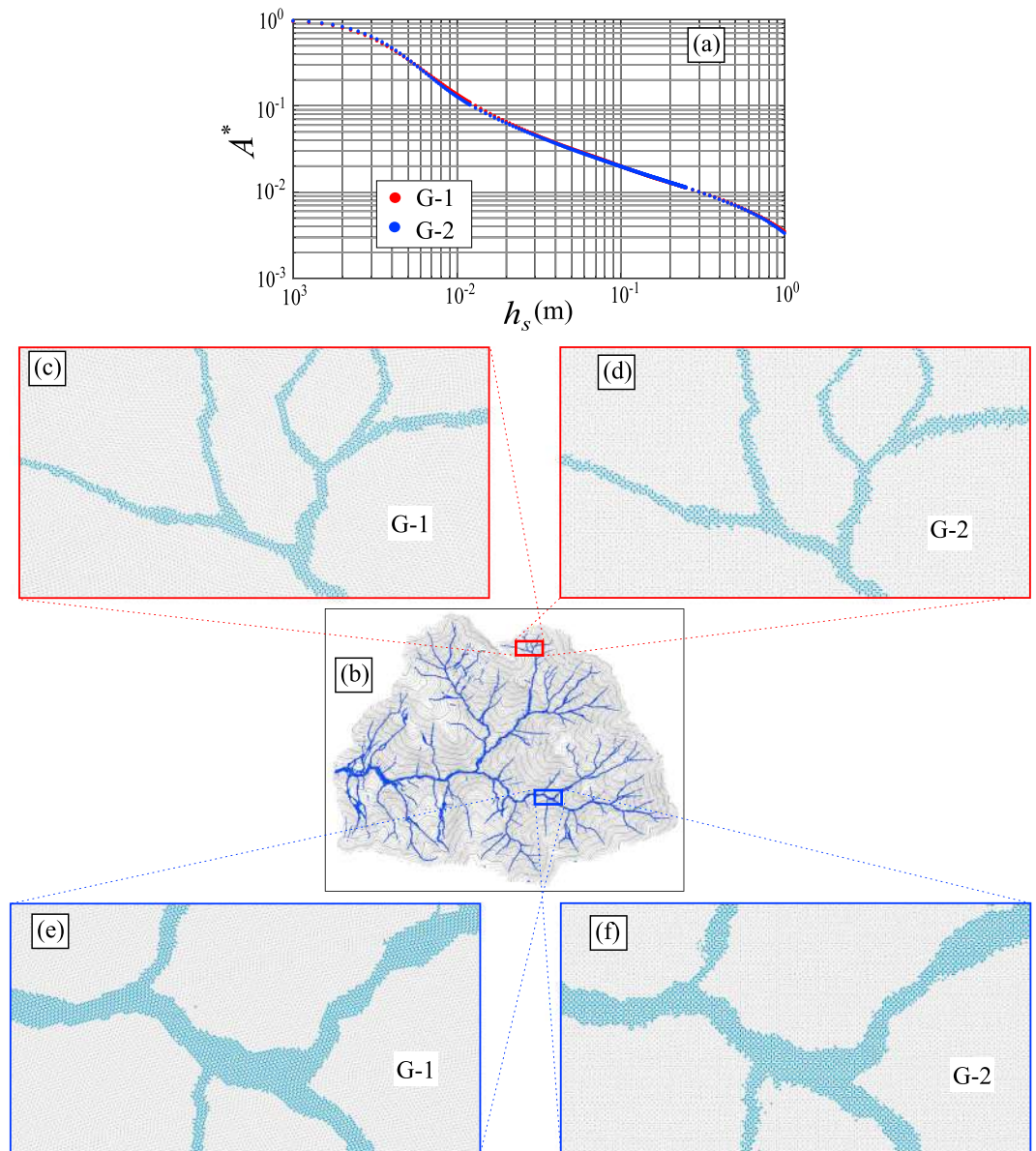


Figure 12. ER1 drainage basin: effects of computational grid on the bimodal scaling law (a) and some details in terms of *net* – *points* organization for a given value of h_s (b–f).

only the basin for which the differences are largest has been shown, it can be observed that the HCN structures are practically superimposed, while some slight differences can be observed in the CN structures. The little influence of the variable s on the $A^* - h^*$ curve means that the value assumed for this variable is not so important for the purposes of this work.

The second issue discussed here is the influence of the Strickler coefficient values assumed throughout the basins and how much a differentiation between the values assumed for the main channels and hillslopes can affect the scale parameters b . To that purpose, four other simulations have been performed, varying the Strickler coefficient assumed for the shallow flow over hillslopes $K_{s,h}$ (30, 20, 10, and $5 \text{ m}^{1/3}/\text{s}$) keeping the Strickler coefficient constant for the channelized flow ($30 \text{ m}^{1/3}/\text{s}$). In Figure 11b, the four $A^* - h^*$ curves are shown. In particular, the graph refers to the AP1 basin, considered representative of all the situations analyzed in this work. A slight influence on the scale parameter b , characterizing the HCN structures, can be observed from the analysis of Figure 11b, while no significant differences exist for the scale parameter b related to the CN structures. Specifically, the strong variation assumed for $K_{s,h}$ (more than 80%) has induced

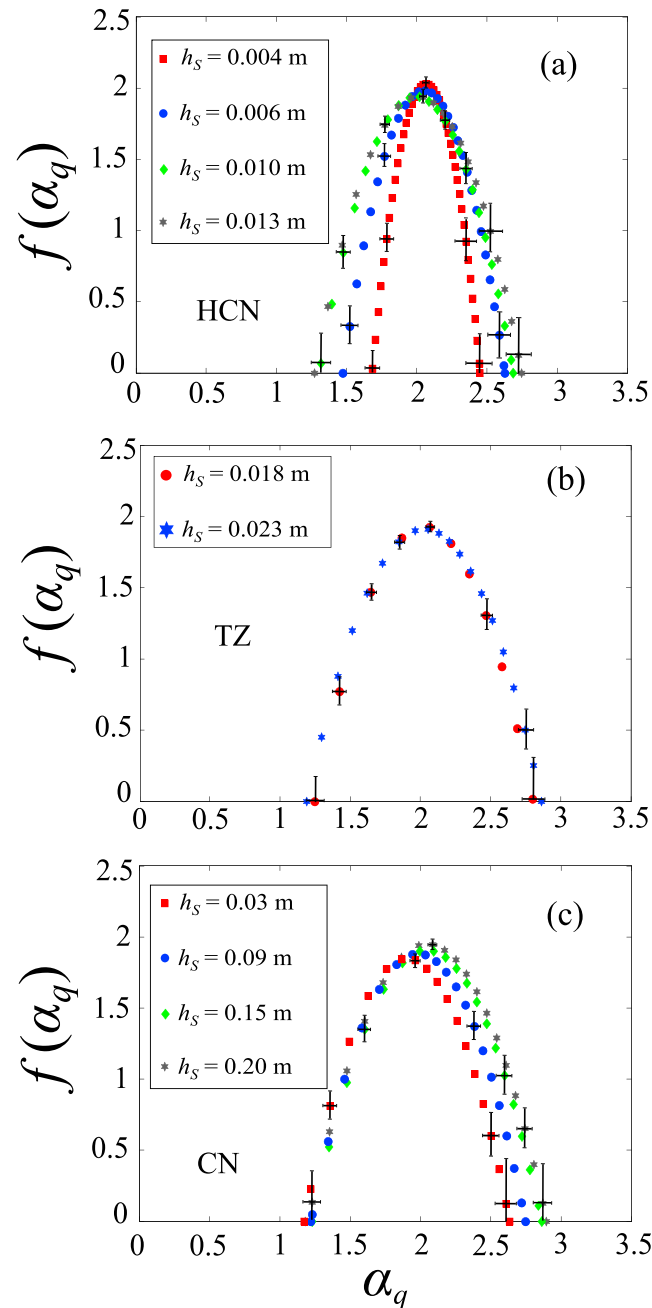


Figure 13. Multifractal spectra of the (a) HCN, (b) TZ, and (c) CN configurations (AP1 basin). HCN = hillslope plus channel networks; TZ = transition zone; CN = channel networks.

a little influence on the values of b for the HCN structures (no more than 15%). Therefore, it may be concluded that a differentiation between the values assumed for the Strickler coefficients for shallow flows over hillslope and channelized flow does not alter, significantly, the bimodal structure of the proposed scaling laws. However, it may be important to observe that, for smaller $K_{s,h}$ values, the whole A^*-h_s curve becomes flatter leading to an extension of the TZ.

Finally, Figure 12 shows the influence of the computational grid on the results. For the sake of brevity, attention has been focused on the ER1 basin only (Figure 12b). In particular, Figure 12a highlights that no significant effects have been played by the computational grid on the bimodal scaling laws. The details

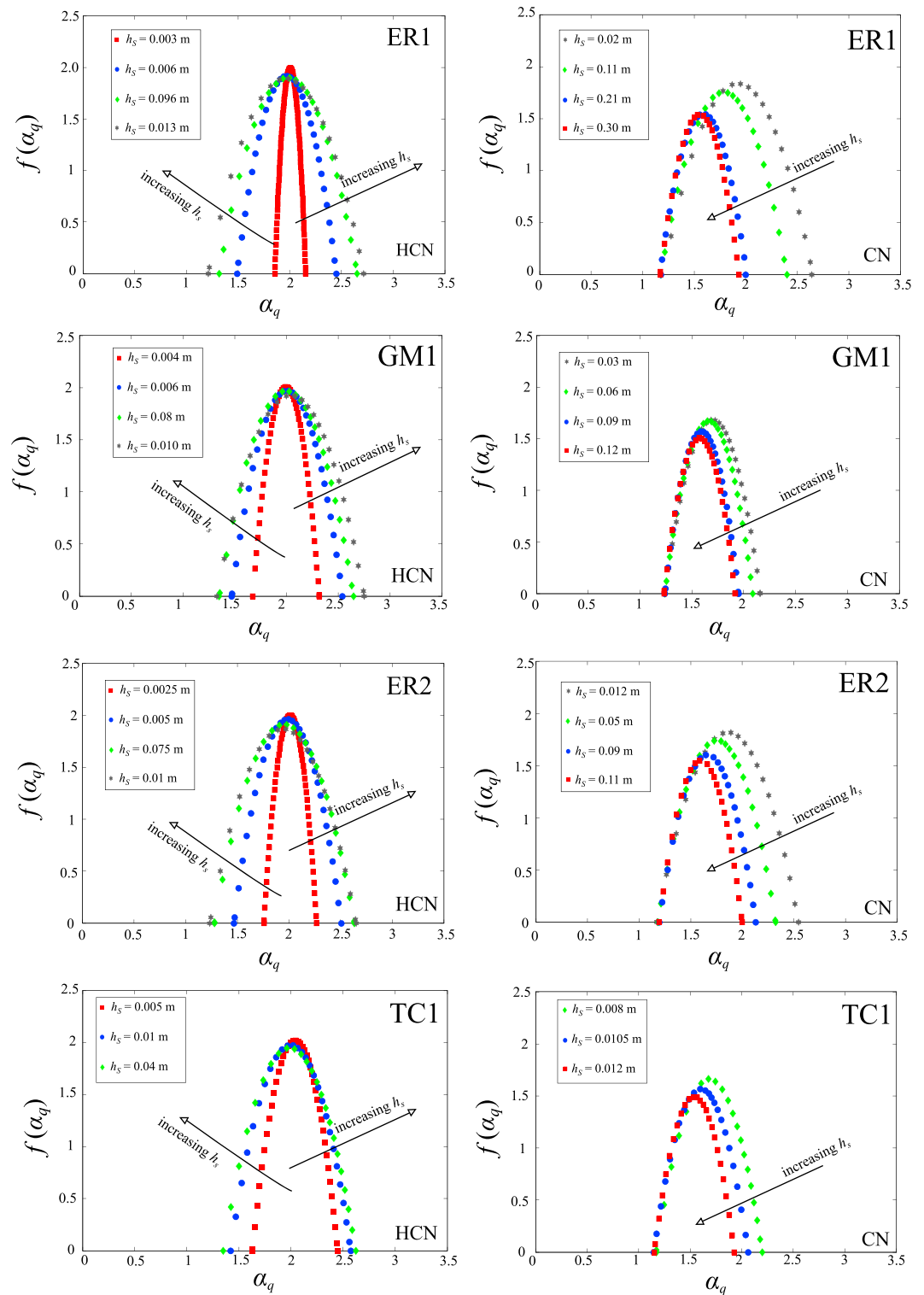


Figure 14. Multifractal spectra of the HCN and CN configurations (ER1, GM1, ER2, and TC1 river basins). HCN = hillslope plus channel networks; CN = channel networks.

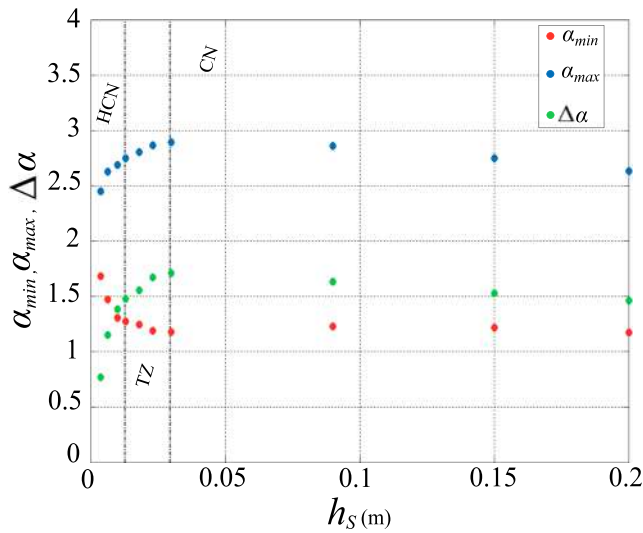


Figure 15. Variation of α_{min} , α_{max} , and $\Delta\alpha$ as a function of h_s , for the AP1 river basin. HCN = hillslope plus channel networks; CN = channel networks.

range and to one third and two thirds of the length of the interval itself. The multifractal spectra, for the HCN, CN, and TZ configurations, relative to the AP1 basin, are shown in Figure 13, while those related to ER1, GM1, ER2, and TC1 are presented in Figure 14 for the HCN and CN structures. As an example, some error bars have been also plotted in Figure 13. The number of *net – points*, N_t , the p_{inf} and p_{sup} prime neighbors values (that represent the limits of the scaling range for the assessment of the mass moments $q(\tau_q)$), the α_{min} , α_0 , and α_{max} , singularity values, the $f(\alpha_0)$, $f(\alpha_1)$, and $f(\alpha_2)$ fractal dimension values, and the spectrum width $\Delta\alpha$ are shown in Tables 3–7. The behavior of the Lipschitz-Hölder coefficients against the water depth values h_s is given in Figure 15, for the AP1 basin solely, which is representative of the profile observed for each analyzed basin.

4.2.1. Multifractal Geometric Properties of the HCN and CN Structures

In the scaling range (I) of the HCN configurations, a first important result, obtained for all the considered basins, is that the estimated fractal dimensions $f(\alpha_0)$, $f(\alpha_1)$, and $f(\alpha_2)$ decrease as the threshold h_s increases. The same behavior has been observed for the α_{min} profile, as further highlighted in Figure 15. Starting from the α_{min} values estimated for all the configurations reported in Tables 3–6, it might be interesting to observe that the minimum singularity exponents, on average, is substantially constant for each basin (1.45). As

represented in Figures 12c–12f show only some slight differences in terms of *net – points* structures that do not modify, in practice, the observed branching structure.

4.2. Geometric Properties of the Flow Patterns Simulated by the 2-D SWEs: A Fixed Mass Multifractal Analysis

What we want to convey through this section is a physical interpretation of the differentiation between the HCN and CN structures, by characterizing the nature of these two configurations from a geomorphic point of view. In particular, the issue that we are posing now is the following: Can specific geometric features be defined for both the HCN and the CN structures? or, in other words, do some geometric differences exist between the HCN and the CN structures? The answer to these questions will represent the theoretical framework to provide geomorphological explanations of the different processes that characterize the two parts of the $A^* - h_s$ curve, presented in the next section (4.3).

With regard to the HCN and CN configurations, for each analyzed basin, we have estimated the multifractal spectra of four network configurations in the ranges $[h_{s,inf}, h_{s,sup}]_I$ and $[h_{s,inf}, h_{s,sup}]_{II}$. Generally, these configurations are related to the h_s values corresponding to the extremes of the

Table 3

Multifractal Properties of HCN and CN Structures Evaluated for AP1 River Basin

h_s (m)	N_t	p_{inf}	p_{sup}	α_{min}	α_0	α_{max}	$f(\alpha_0)$	$f(\alpha_1)$	$f(\alpha_2)$	$\Delta\alpha$
HCN configuration (mean values: $\alpha_{min} = 1.433$, $\alpha_{max} = 2.628$)										
0.004	2,154,269	1,753	125,179	1.683	2.067	2.452	2.000	1.998	1.956	0.769
0.00625	1,030,604	1,201	135,876	1.473	2.049	2.626	1.983	1.941	1.816	1.153
0.01	463,270	580	129,738	1.305	1.996	2.688	1.940	1.879	1.694	1.383
0.013	325,733	908	69,272	1.271	2.009	2.748	1.939	1.869	1.658	1.477
TZ configuration										
0.018	236,500	764	52,298	1.248	2.026	2.803	1.929	1.851	1.616	1.554
0.023	198,537	4,149	24,736	1.192	2.028	2.864	1.913	1.821	1.547	1.672
CN configuration (mean values: $\alpha_{min} = 1.200$, $\alpha_{max} = 2.785$)										
0.03	172,548	1,162	22,019	1.181	2.038	2.895	1.908	1.812	1.523	1.714
0.09	121,813	948	9,317	1.229	2.046	2.862	1.906	1.819	1.557	1.633
0.15	105,115	656	11,011	1.219	1.983	2.747	1.883	1.806	1.574	1.528
0.20	95,264	354	7,691	1.173	1.904	2.635	1.845	1.773	1.556	1.462

Note. HCN = hillslope plus channel networks; TZ = transition zone; CN = channel networks.

Table 4
Multifractal Properties of HCN and CN Structures Evaluated for ERI River Basin

h_s (m)	N_t	P_{inf}	P_{sup}	α_{min}	α_0	α_{max}	$f(\alpha_0)$	$f(\alpha_1)$	$f(\alpha_2)$	$\Delta\alpha$
HCN configuration (mean values: $\alpha_{min} = 1.468$, $\alpha_{max} = 2.493$)										
0.003	1,528,015	2,081	134,369	1.856	2.000	2.155	1.991	1.988	1.980	0.298
0.006	640,547	1,305	65,341	1.489	1.969	2.449	1.919	1.889	1.798	0.960
0.0096	323,596	904	27,219	1.317	1.985	2.652	1.901	1.843	1.667	1.335
0.013	226,336	746	27,575	1.210	1.963	2.716	1.892	1.817	1.592	1.506
TZ configuration										
0.015	195,908	1,686	10,030	1.195	1.931	2.668	1.885	1.813	1.597	1.473
0.017	174,412	1,570	9,186	1.179	1.921	2.662	1.870	1.797	1.576	1.483
CN configuration (mean values: $\alpha_{min} = 1.173$, $\alpha_{max} = 2.244$)										
0.02	150,943	1,923	6,157	1.169	1.905	2.641	1.845	1.771	1.551	1.472
0.11	44,721	2	10	1.177	1.788	2.400	1.756	1.702	1.543	1.223
0.21	30,100	1	4	1.175	1.588	2.000	1.562	1.535	1.453	0.825
0.3	24,197	2	5	1.171	1.553	1.934	1.539	1.515	1.445	0.762

Note. HCN = hillslope plus channel networks; TZ = transition zone; CN = channel networks.

regards the maximum singularity exponents α_{max} , an increase of these values with the increase of h_s was observed. Similarly to the analysis of the mean values of α_{max} , it might be interesting to observe that the maximum singularity exponents, on average, is substantially constant for each basin (2.56). Moreover, it is important to note that the variation of the α_{min} and α_{max} values, with the increase of h_s , seems to reduce significantly when approaching the large h_s end of the HCN scaling range (see Figures 13 and 14). Finally, it is important to note that the $\Delta\alpha$ amplitude values increase when h_s increases too.

As regards the scaling range (II) of the CN configurations, the analysis of the multifractal properties highlights, also in this case, a systematic decrease of the estimated fractal dimensions $f(\alpha_0)$, $f(\alpha_1)$, and $f(\alpha_2)$ as the threshold h_s increases. Contrarily to the HCN structures, the maximum singularity exponents, α_{max} , decrease as h_s increases, while the minimum singularity exponents α_{min} can be considered quite constant (see Figures 13–15). The physical meaning of the asymmetry observed in the variation between the maximum and minimum singularity exponents will be explained in section 4.3. Moreover, it is interesting to observe that the $\Delta\alpha$ amplitude values decrease when h_s increases, resulting in an opposite behavior in respect to HCN structures.

Table 5
Multifractal Properties of HCN and CN Structures Evaluated for GMI River Basin

h_s (m)	N_t	P_{inf}	P_{sup}	α_{min}	α_0	α_{max}	$f(\alpha_0)$	$f(\alpha_1)$	$f(\alpha_2)$	$\Delta\alpha$
HCN configuration (mean values: $\alpha_{min} = 1.456$, $\alpha_{max} = 2.564$)										
0.004	1,012,360	433	68,165	1.675	1.995	2.316	2.000	1.995	1.956	0.642
0.006	479,620	429	10,427	1.468	2.004	2.540	1.972	1.936	1.827	1.072
0.008	278,055	133	32,707	1.351	1.999	2.647	1.969	1.915	1.756	1.296
0.010	201,554	945	2,310	1.329	2.040	2.751	1.926	1.861	1.664	1.422
TZ configuration										
0.012	166,364	352	4,931	1.302	1.947	2.592	1.847	1.790	1.621	1.291
0.014	146,441	58	25,686	1.277	1.935	2.592	1.828	1.769	1.591	1.315
CN configuration (mean values: $\alpha_{min} = 1.237$, $\alpha_{max} = 2.028$)										
0.030	94,105	466	4,357	1.241	1.700	2.159	1.683	1.652	1.558	0.918
0.060	70,490	688	2,686	1.240	1.663	2.086	1.672	1.645	1.565	0.847
0.090	60,037	366	7,015	1.237	1.592	1.948	1.571	1.551	1.490	0.711
0.120	52,966	990	2,194	1.232	1.575	1.918	1.507	1.487	1.428	0.686

Note. HCN = hillslope plus channel networks; TZ = transition zone; CN = channel networks.

Table 6
Multifractal Properties of HCN and CN Structures Evaluated for ER2 River Basin

h_s (m)	N_t	P_{inf}	P_{sup}	α_{min}	α_0	α_{max}	$f(\alpha_0)$	$f(\alpha_1)$	$f(\alpha_2)$	$\Delta\alpha$
HCN configuration (mean values: $\alpha_{min} = 1.433$, $\alpha_{max} = 2.515$)										
0.0025	332,430	1,251	8,046	1.757	2.012	2.268	2.000	1.992	1.967	0.511
0.0050	144,536	7,969	345	1.464	1.985	2.507	1.963	1.929	1.825	1.042
0.0075	73,827	707	10,890	1.279	1.955	2.633	1.911	1.851	1.671	1.354
0.0100	50,050	707	4,654	1.233	1.941	2.651	1.868	1.801	1.599	1.418
CN configuration (mean values: $\alpha_{min} = 1.186$, $\alpha_{max} = 2.249$)										
0.012	40,955	386	24,395	1.174	1.859	2.545	1.819	1.755	1.561	1.370
0.050	11,772	7	77	1.182	1.752	2.323	1.743	1.696	1.556	1.141
0.090	6,902	5	48	1.195	1.662	2.129	1.605	1.571	1.496	0.934
0.110	5,709	4	29	1.194	1.597	1.999	1.548	1.522	1.444	0.805

Note. HCN = hillslope plus channel networks; CN = channel networks.

4.2.2. Multifractal Geometric Properties of the TZ Structures

A multifractal analysis relative to two river networks belonging to the range $]h_{s,inf}, h_{s,sup}[$ has been carried out (see Figures 8,E and F, and 13b). Figure 13b highlights that the spectra are practically superimposed. In the TZ structures, therefore, the process highlighted for the HCN structures, related to both the increase of α_{max} and the decrease of α_{min} , is stopped. The α_{min} values tend to be stabilized, as is common for CN configurations, while the α_{max} values are no longer increasing, with the increase of h_s , since it is going to start the CN behavior characterized by a reduction of the maximum Lipschitz-Hölder coefficients. The constant behavior assumed by the Lipschitz-Hölder coefficients has been somewhat observed in the analyses of the multifractal spectra relative to the HCN structure. This means that it is not very simple to locate precisely the end of the first scaling range and the beginning of the TZ. It seems important to recall that the TZ configurations are evident only for the analyzed basins that have areas greater than 1 km² (AP1, ER1, and GM1), while they are not observed in the smaller basins (ER2 and TC1).

4.3. Physical and Geomorphological Interpretation of the Bimodal Scaling Law Based on the Variations in the Multifractal Signatures

In this section, we will show the importance of the multifractal analysis performed in the previous section. In particular, on the basis of the variations in the multifractal signatures that have been previously highlighted, we will provide physical and geomorphological interpretations of the HCN and CN structures and, therefore, of their different behavior highlighted in the bimodal scaling law derived from numerical computations only.

For the sake of brevity, this kind of explanation will be presented only for the ER1 basin. The bimodal scaling laws, the arrangements of the *net-points*, and the multifractal spectra related to some values of h_s are shown in Figures 16 (CN behavior) and 17 (HCN behavior).

Table 7
Multifractal Properties of HCN and CN Structures Evaluated for TC1 River Basin

h_s (m)	N_t	P_{inf}	P_{sup}	α_{min}	α_0	α_{max}	$f(\alpha_0)$	$f(\alpha_1)$	$f(\alpha_2)$	$\Delta\alpha$
HCN configuration (mean values: $\alpha_{min} = 1.468$, $\alpha_{max} = 2.548$)										
0.005	55,079	1,324	11,147	1.632	2.004	2.449	2.000	1.999	1.937	0.817
0.01	21,737	102	345	1.421	1.997	2.574	1.976	1.934	1.808	1.153
0.015	12,236	62	196	1.351	1.986	2.623	1.948	1.897	1.741	1.272
CN configuration (mean values: $\alpha_{min} = 1.162$, $\alpha_{max} = 2.061$)										
0.04	4,061	237	1,474	1.171	1.685	2.199	1.662	1.623	1.503	1.028
0.08	2,523	173	452	1.164	1.610	2.057	1.572	1.540	1.445	0.893
0.12	1,862	32	68	1.152	1.540	1.928	1.491	1.466	1.390	0.776

Note. HCN = hillslope plus channel networks; CN = channel networks.

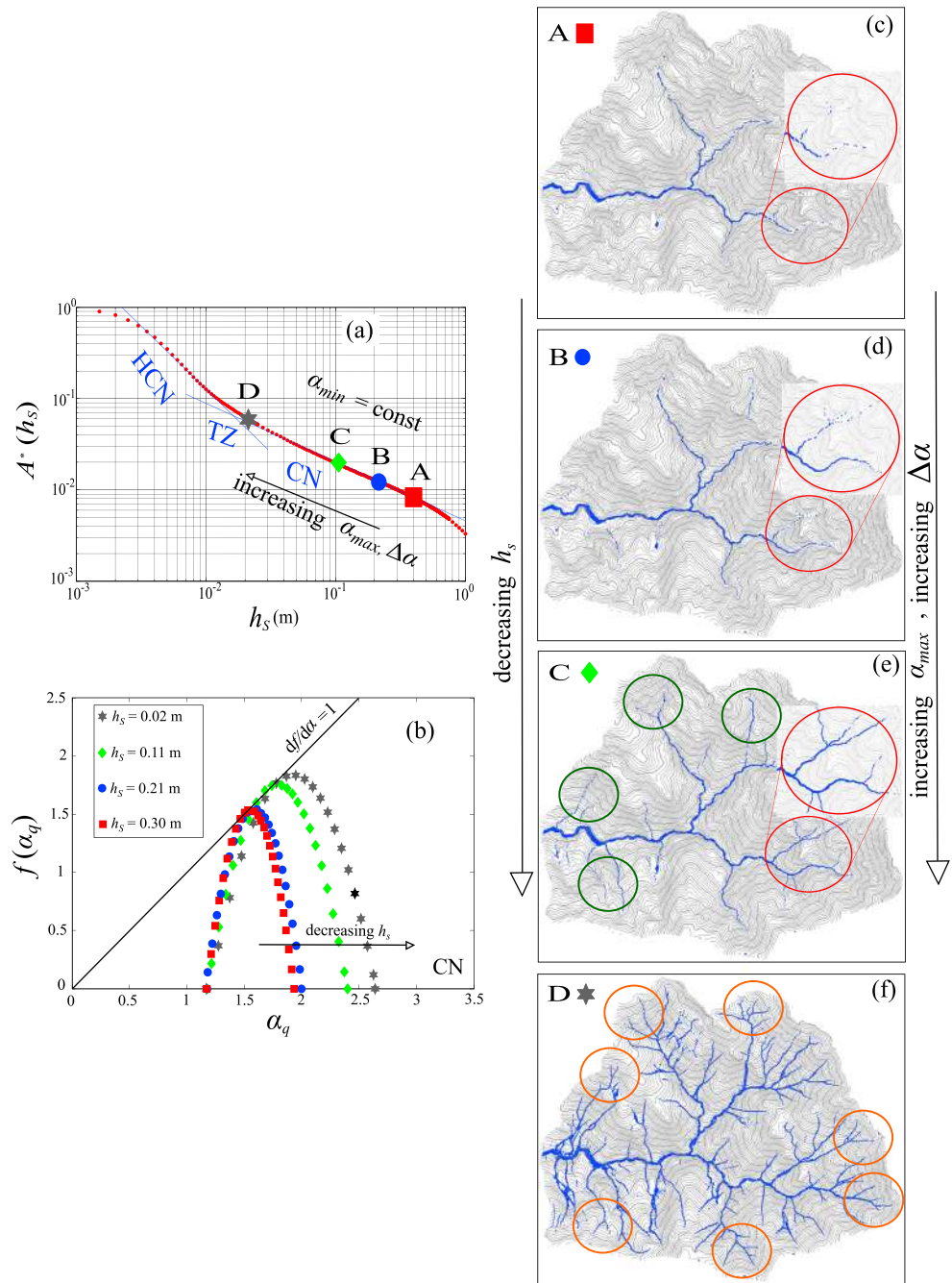


Figure 16. ER1 drainage basin: geomorphological interpretation of the CN part of the $A^* \cdot h_s$ curve (a) on the basis of the estimated multifractal spectra (b); branching process evolution (c–f). HCN = hillslope plus channel networks; TZ = transition zone; CN = channel networks.

As already highlighted in the previous section, the CN structures are characterized by a process represented, from a multifractal point of view, by the increase of α_{max} and $\Delta\alpha$ as h_s decreases, while the α_{min} values are constant. The geomorphological information that we can deduce from these elements is described in what follows.

Following the process using the decreasing values of h_s , the first value of the water depth threshold is represented by the red square in Figure 16a, to which is associated the spectrum with the same symbol in Figure 16b and the *net – points* structure in Figure 16c. The *net – points* arrangement (Figure 16c) describes the main course of the river and two tributaries. This configuration does not change significantly

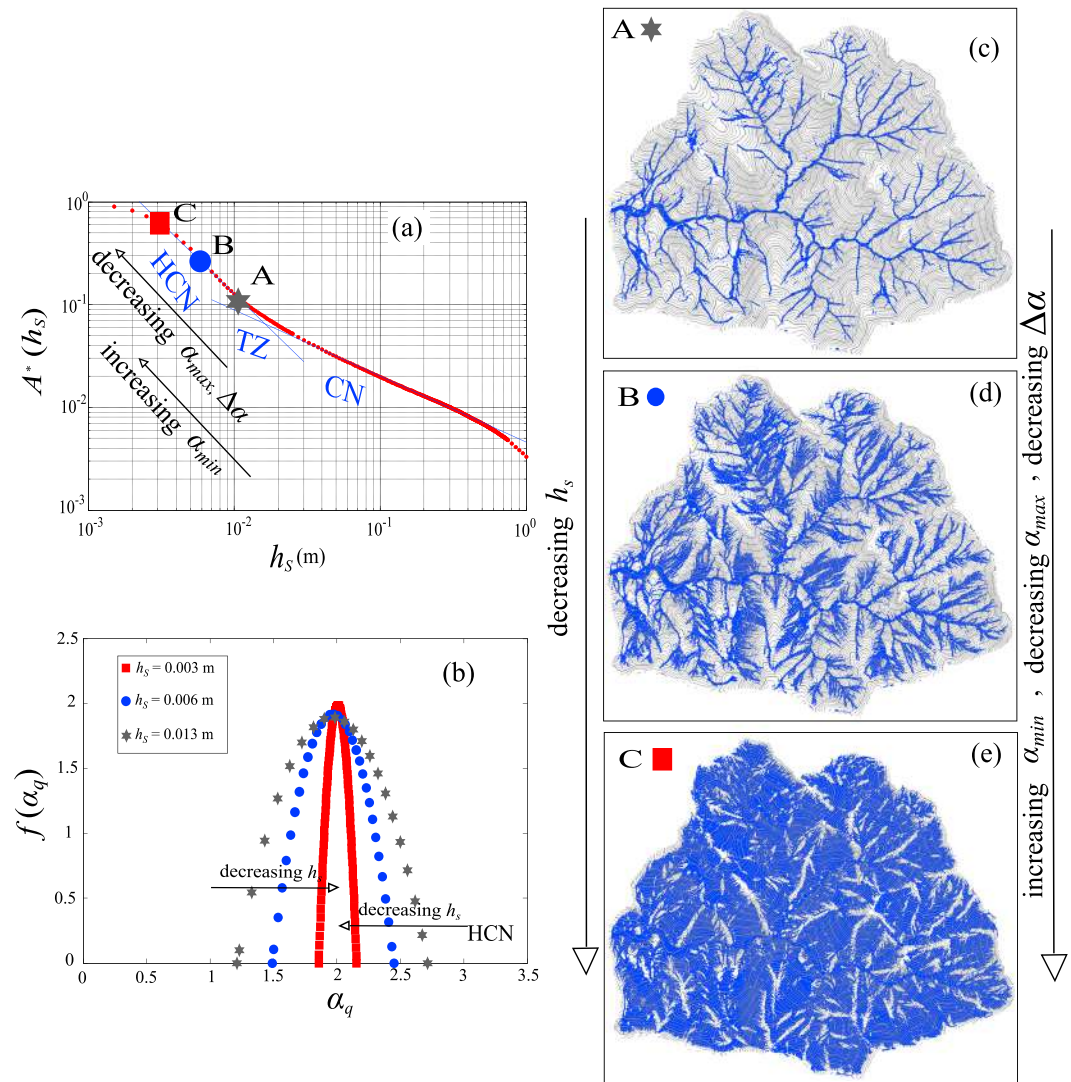


Figure 17. ER1 drainage basin: geomorphological interpretation of the HCN part of the A^*-h_s curve (a) on the basis of the estimated multifractal spectra (b); overland flow process (c,d) and plane-filling behavior (e). HCN = hillslope plus channel networks; TZ = transition zone; CN = channel networks.

(Figure 16d) when considering a smaller value of h_s , represented with a blue circle in Figure 16a, even though it is evident that the streams do fill in when moving from Point A to Point B. It is interesting to observe that the two spectra associated to these two configurations (red squares and blue circle in Figure 16b) are substantially similar to each other, despite a slight increase of α_{max} . This means that two similar structures have similar multifractal spectra, confirming the fact that the spectrum can be considered a measure of the geometrical complexity of the river networks. The slight increase of α_{max} can be explained recalling the physical meaning of this quantity (see equation (3)). Since it is related to the minimum probability and, therefore, to the areas in which the rarefaction of the measure is greater, α_{max} is representative of the peripheral parts of the network (see also Figure 7). The increase of α_{max} implies the decrease of p_{min} because, despite the quite limited increase of the total number of the *net - points*, which in turn gives a limited increase of A^* observed in the scaling law A^*-h_s , there is a significant increase of the minimum number of points (rarefaction) in the far end of the peripheral branches.

In order to better understand the geomorphological situation described by these spectra, we will present a reasoning in which the size of the elements covering the set is fixed a priori ($\epsilon_i = \epsilon$, for every i). Focusing the attention on the density of points falling within the red circles represented in Figures 16c and 16d, as h_s decreases, a slight increase of the points belonging to those areas can be observed, configuring bifurcation

and junctions in the peripheral parts of the network. Following the dual reasoning of the previous one, that is fixing a priori the number of points and, thus p_{\min} , the increase of α_{\max} implies a greater minimum value of ϵ that means the lengthening of the existing water courses, in line with what has been observed by Schroeder (1996) on the characterization of generalized dimensions.

The geomorphological process described by the spectra evolution, as h_s decreases, occurs by keeping the value of α_{\min} constant, which means that no variation exists in terms of maximum probabilities, which are strictly connected with the description of the channelization process in the main river courses. Therefore, the slight increase of α_{\max} induces the slight increase of $\Delta\alpha$ that means, as recalled in section 3.2, a greater heterogeneity (rich in structures) of the river network.

The process described so far, related to the small geometrical and geomorphological differences between the networks associated to the Points A and B belonging to the end of the A^*-h_s law, becomes significantly more evident as h_s decreases, considering, for example, the configuration related to the Point C represented by a green diamond in Figures 16a and 16b. In particular, Figure 16b shows a pronounced increase of α_{\max} and $\Delta\alpha$, while α_{\min} remains unchanged. Compared to the situation represented in Figure 16d, the red circle depicted in Figure 16e allows us to appreciate the significant development of the branching structure and the lengthening of the peripheral parts of the network and, globally, the description of all the minor tributaries highlighted within the green circles. Therefore, the *net – points* structure is characterized by a greater heterogeneity, detected by the increasing value of $\Delta\alpha$. The branching evolution process is completed close to the Point D, represented by the gray star in Figures 16a and 16b, in which the maximum value of α_{\max} and the maximum width $\Delta\alpha$ are reached. Therefore, this configuration represents the maximum heterogeneity of the river network, for the CN structures, as highlighted, for example, by the orange circles in Figure 16f.

Finally, the specific behavior of the CN spectra, symmetrical and tangential to the line

$$\frac{df}{d\alpha} = q = 1 \quad (6)$$

denotes structures of *net – points* typical of a self-similarity set (Feder, 1988; Falconer, 1990, 1997).

Therefore, the physical interpretation of the increase of A^* , as h_s decreases, could be provided in terms of α_{\min} and α_{\max} profiles. The process described by the part CN of the scale law A^*-h_s represents the progressive formation of a more and more complex branching structure characterized by both the lengthening of the peripheral part of the network and the increase of bifurcations, as highlighted by the increasing profile assumed by α_{\max} and $\Delta\alpha$. As a consequence, there is the increase of A^* , but it cannot be very pronounced because the maximum density of *net – points* remains unchanged, as highlighted by α_{\min} that represents the quantity related to the description of the main courses, where the density of measure is greater.

It is important to highlight that the interpretation of the results provided so far is in perfect agreement with the results obtained by De Bartolo, Primavera, et al. (2006), in the context of the characterization of multifractal spectra related to streams of different Horton-Strahler orders, the network for which has been extracted from digitized maps on a 1:25,000 scale.

Neglecting the TZ in which the spectra tend to be superimposed, the decrease of h_s induces a significant steepening of the relation A^*-h_s in a log-log plot. The sudden change of the scale parameter b should be clearly associated to a significant different process that, once again, can be interpreted in the light of the variations in the multifractal signatures. Contrary to the CN structures, the decrease of h_s here implies the change of the sign of the α_{\max} and $\Delta\alpha$ variations (from increasing to decreasing values), while α_{\min} is no longer constant since its variation is positive. Following the process according to the decreasing direction of h_s , the first value considered is the gray star in Figure 17a (Point A), to which is associated the spectrum highlighted by the same symbol in Figure 17b and the *net – point* structure of Figure 17c. At first sight, this configuration is not so different from that shown in Figure 16f, and therefore, the spectrum related to this point is comparable to that associated to the Point D in Figure 16, despite there being small differences. This confirms what has been already underlined about the uncertainties related to the location of the TZ based on the bimodal behavior of the scaling law A^*-h_s , that, instead, can be effectively detected more precisely by analyzing the opposite values assumed by the variation of the spectrum width $\Delta\alpha$.

The situation changes significantly with the decrease of h_s , as highlighted by the Point B in Figure 17a (blue circle) to which corresponds the spectra (same symbols) and the *net – points* structures represented

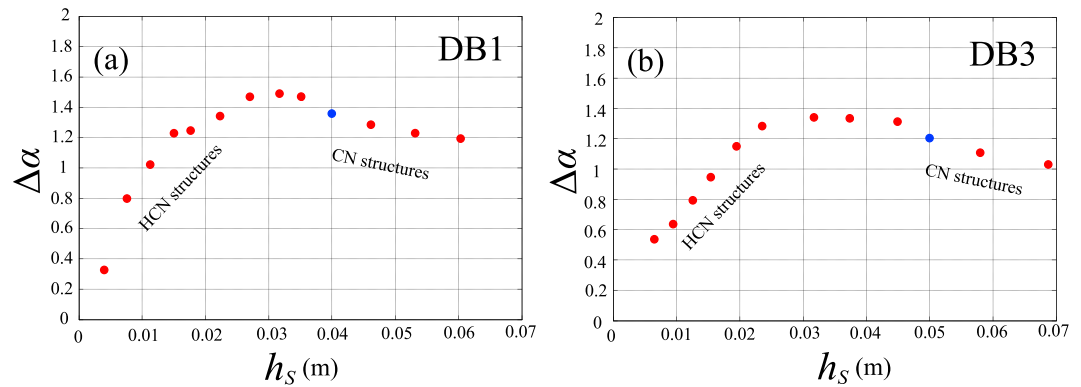


Figure 18. $\Delta\alpha - h_s$ curve estimated for DB1 basin (a) and DB3 basin (b). The blue circles locate the h_s values that identify the river networks, simulated by the 2-D shallow water equations model, used to check the channel heads position. HCN = hillslope plus channel networks; CN = channel networks.

in Figures 17b and 17d. The increase of α_{min} means the decrease of p_{max} , that is, keeping constant ϵ , the maximum number of points falling in the covering box over the total number of the *net - points*. It is evident that the reason for this behavior cannot be found in some modification of the channelization process, already completed in the CN part of the scaling law. Actually, the overland flow process on hillslopes has been activated, combining its effect with the fully developed branching phenomenon in the CN part of the $A^* - h_s$ law. In particular, overland flow on hillslope, by its very nature, cannot be collected in channels that, in turn, are confined in small areas of the basin and are characterized by a limited number of computational cells (*net - points*). Therefore, the overland flow process involves a significantly greater number of computational cells, leading to a drastic increase of the *net - points* that means a rapid increase of A^* . So the increase of the denominator and the substantially constant value of the numerator, which analytically define p_{max} , explain the increase of α_{min} , as the result of the activation of overland flow process. A similar reasoning can be followed to justify the decrease of α_{max} and the consequent increase of p_{min} . Specifically, due to the very low values assumed by h_s , all the peripheral parts of the basin are involved, leading to a rapid increase of the minimum number of points falling into a covering box. This increment exceeds that associated to the total number of *net - points*, and therefore, we have an increase of p_{min} and a decrease of α_{max} .

The relevance of the phenomenon just described becomes more and more important with the decrease of h_s , as highlighted by the Point C of Figure 17a (see red square) to which corresponds the spectrum depicted with the same symbol and the *net - points* structure highlighted in Figures 17b and 17e, respectively. The latter figure, in particular, shows that the further decrease of h_s implies the generation of *net - points* practically everywhere in the basin, leading to a plane-filling behavior. This fact is confirmed by the associated spectrum that is characterized by $f(\alpha_0)$ substantially equal to α_0 . So the fractal dimension of the support is equal to 2, typical of a river structure widely homogeneous in the plane. Following a reasoning based on increasing the value of h_s in the HCN part of the $A^* - h_s$ law, it is evident that the homogeneity of the structure is progressively less significant, leading to a more and more heterogeneous aggregation of *net - points* as highlighted, quantitatively, by the increase of the spectra width $\Delta\alpha$.

5. Perspective for Channel Heads Detection

The question that we are posing now is how the findings of this research could be nested in the general framework related to channel heads detection.

A stream channel head is the upstream boundary of concentrated water flow and sediment transport between definable banks (Dietrich & Dunne, 1993) and represents the transition from unchanneled valley to channel (Montgomery & Foufoula-Georgiou, 1993). Channels are initiated where a valley head generates overland flow of sufficient depth to erode and maintain a channel on the existing ground slope (Abrahams, 1984). According to the foundational studies on this topic (see, e.g., Howard, 1994; Montgomery & Dietrich, 1988; Montgomery & Foufoula-Georgiou, 1993), valleys are commonly associated with convergent topography in the landscape, while channels are identified as sections of valleys constrained by well-defined banks.

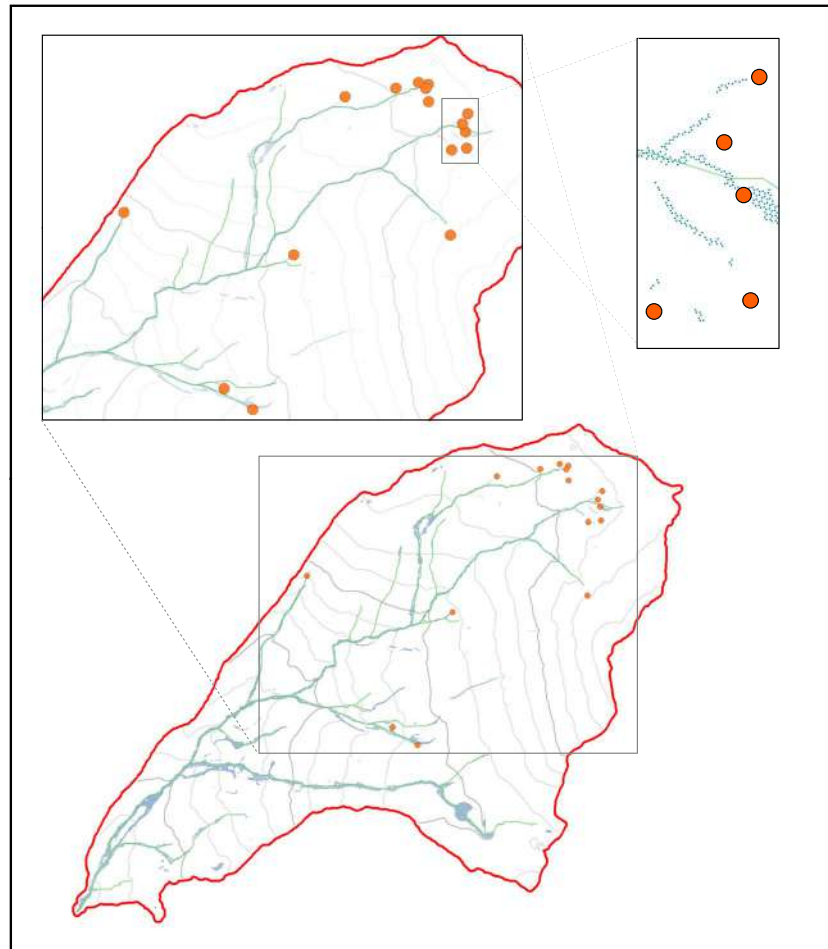


Figure 19. *Net – points* simulated by the 2-D shallow water equations using the proposed criterion based on the $\Delta\alpha-h_s$ curve (blue squares), channel heads location from field observations (orange circles), and the channel network simulated by the best methods considered in Orlandini et al. (2011; green lines): DB1 basin.

Issues related to channel initiation and detection have been extensively studied in the literature (see, e.g., Tarolli, 2014; Wohl, 2018, for a review).

Attention in this section is focused on the field observations of channel heads collected in the eastern Italian Alps (DB1 and DB3), which have been presented in Orlandini et al. (2011). We have chosen these two basins because they are recognized as difficult cases for the prediction of channel heads (Orlandini et al., 2011). In that paper, the authors evaluated the performances of state-of-the-art methods for the delineation of drainage basin and surface flow paths (Orlandini & Moretti, 2009; Orlandini et al., 2003), using the D8-LTD approach for surface flow paths and three different methods that define a threshold condition for channel initiation.

The procedure that we have used to analyze the prediction of channel heads location can be summarized according to the following steps: (1) run the 2-D SWEs model, initialized by a given fictitious inflow s and variable roughness throughout the basin, according to what has been explained in section 3.1.2; (2) analyze the multifractal spectra for both HCN and CN configurations, using the Fixed Mass Approach (FMA); and (3) choose the reference network to be used for channel heads detection on the basis of a novel criterion based on the analysis of the $\Delta\alpha-h_s$ curve.

Specifically, as regards the third point, it could be interesting to observe that the A^*-h_s curve could be used to select the specific *net – points* structure to use for channel heads detection. However, as recalled in section 4.2.2, some uncertainties exist in the identification of the TZ and CN zones. Therefore, it can only give a range of values between the TZ area and the left part of the CN line in which the specific value of h_s

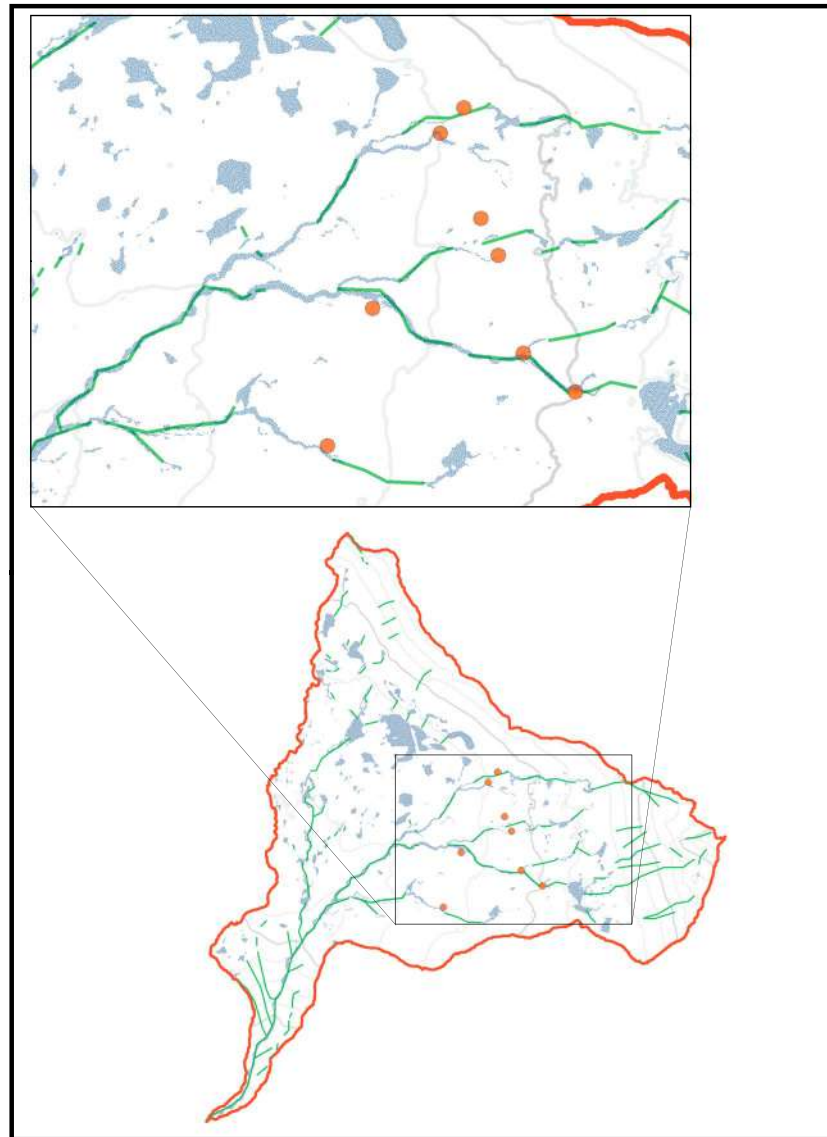


Figure 20. *Net – points* simulated by the 2-D shallow water equations using the proposed criterion based on the $\Delta\alpha-h_s$ curve (blue squares), channel heads location from field observations (orange circles), and the channel network simulated by the best methods considered in Orlandini et al. (2011; green lines): DB3 basin.

can be found, as already highlighted by Figure 9, but no quantitative element can be obtained by that curve to find out the most suitable one. On the contrary, this quantitative indication can be extracted from the $\Delta\alpha-h_s$ curve on the basis of the variation in the multifractal signatures between the HCN and CN structures. In particular, as discussed in sections 4.2.1 and 4.2.2, the increase of h_s leads to a variation of the spectrum amplitude $\Delta\alpha$, given by the difference between α_{max} and α_{min} , inducing a different effect on their values: The $\Delta\alpha$ values increase for the HCN structures and decrease for the CN configurations.

This observation can be used as a potential criterion for the selection of that specific river network configuration, among those ones obtained by the variation of the water depth threshold, to be used for channel heads detection. In particular, a typical $\Delta\alpha-h_s$ curve is represented essentially by three parts (see also Figure 15): the first one in which the $\Delta\alpha$ values increase (HCN configurations), then the second one characterized by reasonably constant values (equal to the maximum $\Delta\alpha$ value), and, finally, a descending part, representing the CN configurations. Therefore, the criterion that we use here is based on the selection of that river network associated to the threshold value located in the descending part of the $\Delta\alpha-h_s$ curve, just after the maximum value, in which a significant decrease of the $\Delta\alpha$ values starts to be observed.

The $\Delta\alpha$ - h_s curves, for both the basins, are reported in Figure 18. In particular, the 2-D SWEs model has been set considering the following values: fictitious net inflow (s) = 50 mm/hr and the Strickler coefficient values equal to 30 and 10 $\text{m}^{1/3}/\text{s}$, for the channels and hillslopes, respectively.

Following the criterion described above, the h_s values corresponding to the blue circles highlighted in Figure 18 have been selected for the comparison with the observed location of the channel heads. In these cases, the river networks simulated by the 2-D SWEs model are represented in Figures 19 and 20, respectively, for DB1 and DB3 basin. In particular, the figures show the simulated *net – points* (blue squares), the observed location of the channel heads (orange circles), and the CN that performed best, among those simulated by Orlandini et al. (2011), according to the evaluations carried out by the authors themselves.

The analysis of Figure 19 highlights that, for the DB1 case, our results show a level of accuracy similar to the best method in Orlandini et al. (2011), based on the computations of the Strahler classification of surface flow paths and pruning the exterior link, even though it seems that the occurrence of channel locations where channels are not observed is lower. As regards the DB3 basin, all the methods considered in Orlandini et al. (2011) overestimate the extension of the CN in the NW part of the drainage basin, where channels are not observed to occur. In any case, in that paper, it is reported that the method that uses a threshold on the function AS^2 , in which A is the drainage area and S the local slope, provided the best results since it did not reproduce a clear CN in the NW part of the basin. Figure 20 refers to the simulated network for the DB3 basin, according to our criterion based on the $\Delta\alpha$ - h_s curve. In particular, there is the tendency to detect channel heads positions where channels have been really observed. As regards the NW part of the basin, the *net – points* corresponding to the selected threshold do not represent a clear CN, configuring a quite fragmented flow connectivity. Considering the level of aggregation of the *net – points*, they seem to describe areas in which the surface runoff is stored, detecting local depressions (artificial or real) that the 2-D SWEs need to fill before the flow continues. In general, the results might be considered similar to or even better than those obtained by Orlandini et al. (2011) considering the method recalled above.

According to the results obtained for the DB1 and DB3 basins, the criterion proposed in this section seems to be a promising and encouraging approach that, however, need further analyses in order to deeply assess the effective potential and limitations.

6. Conclusions

This paper has explored the potential contributions that the SWEs could provide and the intersections that could exist in respect to the traditional analyses devoted to the river basin drainage networks, such as the delineation of channels networks, the scaling laws, and the geometric properties of the river networks from a multifractal point of view.

The main findings of this paper can be grouped in three parts, according to considerations related to scaling properties, their multifractal interpretation, and the novel potential criterion for channel heads detection. They can be summarized as follows:

- (1) The hydraulic characterization of the flow patterns simulated by the 2-D SWEs has been provided by scaling laws that describe the relations between the water depth threshold, used to identify the network cells, and a dimensionless area, defined by the ratio between the total area of the network cells themselves and total basin area.
- (2) The results obtained for five small basins highlighted flow patterns that can be analyzed on the basis of a bimodal scale behavior that has been interpreted here as representative of two different types of river structures: CN and HCN. The analysis of the exponents of the scaling laws highlighted that their differences are quite limited for the HCN structures while they can be much more important for the CN configurations, ranging from 1.4 to 1.7 in the first cases and 0.3–0.8 in the second cases. It might be of interest to highlight also the presence of a TZ, in which the points deviate from the bimodal behavior determined by the scaling laws relative to the HCN and CN configurations.
- (3) The physical and geomorphological interpretation of the bimodal scaling law has been provided from a multifractal point of view to describe the geometric complexity of dense and sparse clusters of the drainage networks. In particular, the analysis of the estimated multifractal spectra highlights significant variations in the multifractal signatures between the CN and the HCN structures. Specifically, the decrease of h_s involves HCN structures characterized by the significant increase of α_{min} and by the

- decrease of both α_{max} and α_{min} . On the contrary, the decrease of h_s involves CN structures for which we have decreasing values for α_{max} and $\Delta\alpha$ while α_{min} is constant.
- (4) The bimodal scaling law has been interpreted in the light of these variations in the multifractal signatures. The configurations belonging to the CN part of the A^*-h_s curve identify *net – points* structures that represent progressively, as h_s decreases, the increase of the river bifurcations and lengthening of the existing water courses. This situation has been demonstrated rigorously by the increase of the α_{max} values and by the simultaneous constant value assumed by α_{min} , that further highlights a substantially similar geometrical description of the main channels. As a consequence, the decrease of h_s induces increasing values of $\Delta\alpha$ leading to a greater heterogeneity of the *net – points* configurations that, being richer in structures, describe progressively the peripheral branches of the river networks. Therefore, the increase of A^* as h_s decreases is explained by the increase of α_{max} . However, it cannot be very pronounced ($b < 1$) because the maximum density of *net – points*, α_{min} , remains unchanged. The sudden change of the scale parameter that characterizes the HCN part of the A^*-h_s curve ($b > 1$) is clearly associated to a significantly different process which is the combination of overland flow on hillslope and the fully developed branching phenomenon that characterizes the CN part of the scaling law. Specifically, it is induced by the drastic increase of α_{min} , which, in turn, is the consequence of the significant increase of the number of *net – points* involved by the activation of overland flow processes.
 - (5) The variations in the multifractal signatures, previously highlighted, have inspired a potential novel criterion for channel heads detection. In the approach proposed here, this means finding a specific value of h_s , that in turn represents a river network configuration simulated by the 2-D SWEs model, able to reproduce the observed channel heads locations. In particular, after a run of the 2-D SWEs model and the computations of the multifractal spectra for the HCN and CN structures, it is possible to select the specific river network associated to the threshold value located in the descending part of the $\Delta\alpha-h_s$ curve, just after the maximum value, in which a significant decrease of the $\Delta\alpha$ values starts to be observed. According to the results obtained for the DB1 and DB3 basins, the criterion proposed in this section seems to be a promising and encouraging approach that, however, requires further analyses in order to deeply assess the effective potential and limitations.

It is important to underline here that these conclusions are somewhat limited by the very small size of the considered basins. Further studies are needed in order to extend these conclusions to bigger basins.

Appendix A: Numerical Scheme

Equation (1) is integrated over an arbitrary control volume Ω_i , and applying Green's theorem to each component of the vectors \mathbf{F} and \mathbf{G} in order to obtain surface integrals, it becomes as reported in equation A1

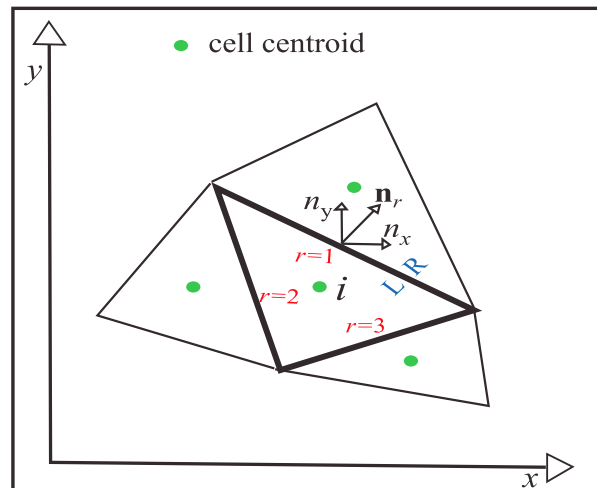


Figure A1. Frame reference for the spatial discretization of the shallow water equations model.

(see, e.g., Hirsch, 1990):

$$\frac{\partial}{\partial t} \int_{\Omega_i} \mathbf{U} d\Omega + \oint_{\partial\Omega_i} [\mathbf{F}, \mathbf{G}] \cdot \mathbf{n} dL = \int_{\Omega_i} (\mathbf{R} + \mathbf{S}) d\Omega, \quad (\text{A1})$$

where $\partial\Omega_i$ is the boundary enclosing Ω_i , \mathbf{n} is the unit vector normal, and L is the length of each boundary. Denoting by \mathbf{U}_i the average value of the flow variables over the control volume Ω_i at a given time, the equation (A1) can be discretized as

$$\mathbf{U}_i^{n+1} = \mathbf{U}_i^n - \frac{\Delta t}{\Omega_i} \sum_{r=1}^3 [\mathbf{F}, \mathbf{G}]_r^n \cdot \mathbf{n}_r \Delta L_r + \Delta t \mathbf{R}_i^n + \Delta t \mathbf{S}_i^n. \quad (\text{A2})$$

The evaluation of the numerical flux in equation (A2) is based on the Riemann problem defined by the conditions on the left (L) and right sides (R) of the cell edges (see Figure A1). Assuming Roe's (1981) approximated Jacobian, the numerical flux across each edge r of the computational cell L on the left and R on the right is

$$[\mathbf{F}, \mathbf{G}]_r \cdot \mathbf{n}_r = \frac{1}{2} \left[[\mathbf{F}, \mathbf{G}]_R \cdot \mathbf{n}_r + [\mathbf{F}, \mathbf{G}]_L \cdot \mathbf{n}_r - \sum_{m=1}^3 |\tilde{\lambda}^m| \alpha^m \tilde{\mathbf{e}}^m \right], \quad (\text{A3})$$

with

$$\alpha^{1,3} = \frac{h_R - h_L}{2} = \pm \frac{1}{2\tilde{c}} \{ [(hu)_R - (hu)_L] n_x + [(hv)_R - (hv)_L] n_y - (\tilde{u} n_x + \tilde{v} n_y) (h_R - h_L) \}, \quad (\text{A4})$$

$$\alpha^2 = \frac{1}{\tilde{c}} \{ [(hv)_R - (hv)_L - \tilde{v} (h_R - h_L)] n_x - [(hv)_R - (hv)_L - \tilde{u} (h_R - h_L)] n_y \}. \quad (\text{A5})$$

$\tilde{\lambda}$ and $\tilde{\mathbf{e}}$ are the eigenvalues and the eigenvectors of the approximated Jacobian matrix defined as follows:

$$\tilde{\lambda}^{1,3} = \tilde{u} n_x + \tilde{v} n_y \pm \tilde{c}; \tilde{\lambda}^2 = \tilde{u} n_x + \tilde{v} n_y; \tilde{\mathbf{e}}^{1,3} = \begin{pmatrix} 1 \\ \tilde{u} \pm \tilde{c} n_x \\ \tilde{v} \pm \tilde{c} n_y \end{pmatrix}; \tilde{\mathbf{e}}^2 = \begin{pmatrix} 0 \\ -\tilde{c} n_y \\ \tilde{c} n_x \end{pmatrix}. \quad (\text{A6})$$

They depend on the following averaged variables:

$$\tilde{u} = \frac{\sqrt{h_R} u_R + \sqrt{h_L} u_L}{\sqrt{h_R} + \sqrt{h_L}}; \tilde{v} = \frac{\sqrt{h_R} v_R + \sqrt{h_L} v_L}{\sqrt{h_R} + \sqrt{h_L}}; \tilde{c} = \sqrt{\frac{g}{2} (h_R + h_L)} \quad (\text{A7})$$

In order to avoid nonphysical discontinuities, the Harten and Hyman (1983) modification of the modulus of eigenvalues $\tilde{\lambda}$ is applied.

The source term vector \mathbf{S} is decomposed in two different parts that are treated separately: the bottom variation \mathbf{S}_0 and the friction term \mathbf{S}_f ($\mathbf{S} = \mathbf{S}_0 + \mathbf{S}_f$). In the upwind schemes, an upwind approach has been adopted to model the bottom variations. For every edge r of the control volume, the inward contribution of the bottom term is (Brufau et al., 2004)

$$\tilde{S}_{0r} = \sum_{m=1}^3 \beta^{m-} \tilde{\mathbf{e}}^m, \quad (\text{A8})$$

where the coefficients β^{m-} are calculated as

$$\beta^{1-,3-} = \pm \frac{1}{4\tilde{c}} \left(1 - \frac{|\lambda_{1,3}|}{\lambda_{1,3}} \right) (\bar{\mathbf{S}}_0^{(2)} n_x + \bar{\mathbf{S}}_0^{(3)} n_y) d_{RL}; \beta^{2-} = \frac{1}{2\tilde{c}} \left(1 - \frac{|\lambda_2|}{\lambda_2} \right) (-\bar{\mathbf{S}}_0^{(2)} n_y + \bar{\mathbf{S}}_0^{(3)} n_x) d_{RL}, \quad (\text{A9})$$

where $\bar{\mathbf{S}}_0^{(2)}$ and $\bar{\mathbf{S}}_0^{(3)}$ are the second and third components of the vector of source terms $\bar{\mathbf{S}}_0$:

$$\bar{\mathbf{S}}_0 = \begin{pmatrix} 0 \\ g\tilde{h}\Delta z_x \\ g\tilde{h}\Delta z_y \end{pmatrix}, \quad (\text{A10})$$

in which $\tilde{h} = 1/2(h_R + h_L)$; $\Delta z_x = -\frac{(z_R - z_L)}{d_{RL}} n_x$; $\Delta z_y = -\frac{(z_R - z_L)}{d_{RL}} n_y$ and d_{RL} is the distance between the centroids of the right (R) and left (L) cells.

A semi-implicit treatment of the friction source term (Brufau et al., 2004; Cea & Bladé, 2015; Costabile et al., 2013) is applied here leading to the following relation:

$$\mathbf{U}_i^{n+1} = \frac{\mathbf{U}_i^* + \Delta t \theta \mathbf{S}_i^n}{1 - (1 - \theta) \Delta t \frac{\mathbf{S}_i^n}{\mathbf{U}_i^n}}, \quad (\text{A11})$$

in which $\mathbf{U}^* = \mathbf{U}_i^n - \frac{\Delta t}{\Omega_i} \sum_{r=1}^3 ([\mathbf{F}, \mathbf{G}]_r^n \cdot \mathbf{n}_r - \tilde{\mathbf{S}}_{0r}^n) \Delta L_r + \Delta t \mathbf{R}_i^n$; θ is the implicitness degree of the friction term discretization: $\theta = 1$ corresponds to a totally explicit treatment and $\theta = 0$ to a totally implicit one. Finally, a robust wet-dry procedure was implemented (for further details, one may refer to Costabile et al., 2013).

Appendix B: Multifractal Formalism and Fixed Mass Approach

A multifractal formalism can be expressed starting from the probability distribution p_i defined in section 3.2.1, introducing the following relations:

$$p_i(\epsilon) = \epsilon_i^\alpha, N_\alpha(\epsilon) = \epsilon_i^{f(\alpha)}, \quad (\text{B1})$$

in which α is a singularity exponent, $N_\alpha(\epsilon)$ is the number of cells where the probability distribution has a singularity between α and $\alpha + d\alpha$, and $f(\alpha)$ is the fractal dimension of the set of cells with the same singularity. Following Halsey et al. (1986), starting from the well-known partition function reported in equation (B2):

$$\sum p_i^q = e^{\tau_q}, \quad (\text{B2})$$

in which τ_q is the sequence of mass exponent and q represents the moments of the measures p_i ; the multifractal spectrum $f(\alpha)$ can be obtained through the Legendre transformation (see equation (B3)):

$$\alpha_q = \frac{d\tau_q}{dq}, f(\alpha_q) = q\alpha_q - \tau_q. \quad (\text{B3})$$

From a numerical point of view, in this work a FMA has been used because, in respect to other available techniques, such as the Fixed Size Algorithms, it presents the advantage of a better estimation of the so-called right side of multifractal spectra which are characterized by negative-weight measures (De Bartolo, Primavera, et al., 2006; Kamer et al., 2013). This latest development allows also a better estimation of the highest singularity indexes of multifractal spectra associated to the minimum probability density of the measures that characterize the river network structures (De Bartolo et al., 2000, 2004; De Bartolo, Primavera, et al., 2006; De Bartolo, Veltri, et al., 2006). This aspect is fundamental in the light of the importance of this quantity as regards the analysis of branching structures.

In the FMAs algorithms, the number of points (or mass) is fixed a priori, and only successively is the minimum radius cell containing all the considered points determined. Therefore, FMA techniques focus on the sequences of distances defined by the prime neighbors for each point of the multifractal river network. The quantity held fixed in the FMAs is the measure p_i inside the i th box, namely, $p_i = p \forall i$ (i.e., $N_i = N \forall i$) and not the size ϵ_i of the covering boxes. The procedure used here is based on the technique presented in De Bartolo, Primavera, et al. (2006) in which the reader can find all the details and theoretical explanations. Starting from the relation B2, it is possible to demonstrate the following relation:

$$\lim_{\epsilon_i \rightarrow 0} \frac{\sum_{i=1}^{N_c} \epsilon_i^{-\tau_q}}{N_c} = k p^{1-q}. \quad (\text{B4})$$

Equation (B4) can be rewritten as reported in equation (B5), introducing the quantity $M(\epsilon_i, \tau_q) = \sum_i \epsilon_i^{-\tau_q} / N_c$ and taking the logarithms of both members of the equation (De Bartolo, Primavera, et al., 2006; Falconer, 1990, 1997; Mach et al., 1995):

$$\lim_{\epsilon_i \rightarrow 0} \ln M(\epsilon_i, \tau_q) = (1 - q) \lim_{p \rightarrow 0} \ln p + \ln k. \quad (\text{B5})$$

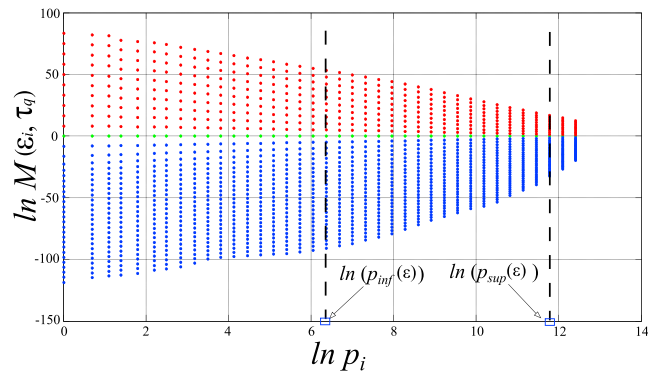


Figure B1. Scaling of $\ln M$ versus $\ln p_i$ and scaling limits used for the numerical computation of equation (B5) (AP1 basin, $h_s = 0.25$ m).

More precisely, once a range of values for τ_q is selected, a set of decreasing values of p is fixed for each τ_q . The range of the sequences of the mass exponent τ_q has been chosen according to the number of the *net* – *points* obtained from the numerical simulation carried out by the SWEs model. This number ranges within 10^3 – 10^6 for the selected basins. Following the suggestion provided by Meneveau and Sreenivasan (1991), regarding the correct estimation of multifractal measures, the selected order of the moment of the measures presented here is about 10^q . Then, the distances $d(x_i, x_j)$ between each point x_i of the *net* – *points* data set and the generic point x_j are computed and sorted in increasing order. The value of ϵ_i for the point under consideration is obtained by the p th value of the $d(x_i, x_j)$ list that is the diameter of a circle containing p points. So it is possible to numerically compute the limit of the equation (B5) through the values of the angular coefficient $(1 - q)$, from the scaling of $\ln M(\epsilon_i, \tau_q)$ versus $\ln p$. In particular, the numerical estimation of the limit has been carried out by selecting the scaling range, as a function of q , delimited by the scaling limits ($\ln(p_{inf})$ and $\ln(p_{sup})$); see Figure B1). The scaling limits have been selected fixing the range of the probability measure according to a process based on maximization of the coefficient of determination R^2 . In this way, the value of q associated to the given τ_q is obtained, and inverting the relation $q = q(\tau_q)$, we have not only the behavior of τ_q as a function of q but also the other related quantities using the Legendre transform, specifically the $f(\alpha_q)$ spectrum. The error propagation bars have been also computed and then propagated through the usual techniques of asymptotic expansion in the determination of the $f(\alpha_q)$.

Acknowledgments

The authors thank Taylor Perron (Massachusetts Institute of Technology, USA), and Stefano Orlandini (Università degli Studi di Modena e Reggio Emilia, Modena, Italy) for providing high-resolution digital elevation model data respectively for the USA basins (GM1 and AP1) and Italian basins (TC1, DB1, and DB3). The DEM data and the simulated water depths can be downloaded online (<https://figshare.com/s/56e11f5b7cd3462f33db>). This work was supported in part by the funding project PON SILA – PONa3_00341A (LaMPIT Laboratory, Scient. Head: F. Macchione). The authors are grateful to the three anonymous reviewers for their remarkable comments that led to significant improvements in the manuscript.

References

- Abrahams, A. D. (1984). Channel networks: A geomorphological perspective. *Water Resources Research*, *20*(2), 161–168.
- Ariza-Villaverde, A. B., Jiménez-Hornero, F. J., & Gutiérrez de Ravé, E. (2013). Multifractal analysis applied to the study of the accuracy of DEM-based stream derivation. *Geomorphology*, *197*, 85–95.
- Ariza-Villaverde, A. B., Jiménez-Hornero, F. J., & Gutiérrez de Ravé, E. (2015). Influence of DEM resolution on drainage network extraction: A multifractal analysis. *Geomorphology*, *241*, 243–254.
- Barber, C. A., & Gleason, C. J. (2018). Verifying the prevalence, properties, and congruent hydraulics of at-many-stations hydraulic geometry (AMHG) for rivers in the continental United States. *Journal of Hydrology*, *556*, 625–633.
- Beck, C. (1990). Upper and lower bounds on the Rényi dimensions and the uniformity of multifractals. *Physica D*, *41*, 67–78.
- Beck, C., & Schlögl, F. (1993). *Thermodynamics of chaotic systems. An introduction*. Cambridge, UK: Cambridge University Press.
- Bellos, V., & Tsakiris, G. (2016). A hybrid method for flood simulation in small catchments combining hydrodynamic and hydrological techniques. *Journal of Hydrology*, *540*, 331–339.
- Bout, B., & Jetten, V. G. (2018). The validity of flow approximations when simulating catchment-integrated flash floods. *Journal of Hydrology*, *556*, 674–688.
- Brufau, P., García-Navarro, P., & Vázquez-Cendón, M. E. (2004). Zero mass error using unsteady wetting-drying conditions in shallow flows over dry irregular topography. *International Journal for Numerical Methods in Fluids*, *45*, 1047–1082.
- Caviedes-Voullième, D., García-Navarro, P., & Murillo, J. (2012). Influence of mesh structure on 2D full shallow water equations and SCS curve number simulation of rainfall/runoff events. *Journal of Hydrology*, *448*, 39–59.
- Cea, L., & Bladé, E. (2015). A simple and efficient unstructured finite volume scheme for solving the shallow water equations in overland flow applications. *Water Resources Research*, *51*, 5464–5486. <https://doi.org/10.1002/2014WR016547>
- Cea, L., Garrido, M., & Puertas, J. (2010). Experimental validation of two-dimensional depth-averaged models for forecasting rainfall-runoff from precipitation data in urban areas. *Journal of Hydrology*, *382*, 88–102.
- Costabile, P., Costanzo, C., & Macchione, F. (2012). Comparative analysis of overland flow models using finite volume schemes. *Journal of Hydroinformatics*, *14*(1), 122–135.
- Costabile, P., Costanzo, C., & Macchione, F. (2013). A storm event watershed model for surface runoff based on 2D fully dynamic wave equations. *Hydrological Processes*, *27*(4), 554–569.

- Costabile, P., Costanzo, C., & Macchione, F. (2017). Performances and limitations of the diffusive approximation of the 2-D shallow water equations for flood simulation in urban and rural areas. *Applied Numerical Mathematics*, *116*, 141–156.
- Costabile, P., & Macchione, F. (2015). Enhancing river model set-up for 2-D dynamic flood modeling. *Environmental Modelling & Software*, *67*, 8–107.
- De Bartolo, S., Dell'Accio, F., Frandina, G., Moretti, G., Orlandini, S., & Veltri, M. (2016). Relation between grid, channel, and Peano networks in high-resolution digital elevation models. *Water Resources Research*, *52*, 3527–3546. <https://doi.org/10.1002/2015WR018076>
- De Bartolo, S., Fallico, C., & Ferrari, E. (2015). Simple scaling analysis of active channel patterns in Fiumara environment. *Geomorphology*, *232*, 94–102.
- De Bartolo, S. G., Gabriele, S., & Gaudio, R. (2000). Multifractal behaviour of river networks. *Hydrology and Earth System Sciences*, *4*(1), 105–112.
- De Bartolo, S. G., Gaudio, R., & Gabriele, S. (2004). Multifractal analysis of river networks: Sand-box approach. *Water Resources Research*, *40*, W02201. <https://doi.org/10.1029/2003WR002760>
- De Bartolo, S. G., Primavera, L., Gaudio, R., D'Ippolito, A., & Veltri, M. (2006). Fixed-mass multifractal analysis of river networks and braided channels. *Physical Review E*, *74*, 026101–1–026101-8.
- De Bartolo, S. G., Veltri, M., & Primavera, L. (2006). Estimated generalized dimensions of river networks. *Journal of Hydrology*, *322*(1–4), 181–191.
- Di Giammarco, P., Todini, E., & Lamberti, P. (1996). A conservative finite elements approach to overland flow: The control volume finite element formulation. *Journal of Hydrology*, *175*, 276–291.
- Dietrich, W. E., & Dunne, T. (1993). The channel head. In K. Beven, & M. J. Kirkby (Eds.), *Channel network hydrology* (pp. 175–219): Wiley.
- Dodds, P. S., & Rothman, D. H. (1999). Unified view of scaling laws for river networks. *Physical Review E*, *59*, 4865–4877.
- Dodov, B., & Fofoula-Georgiou, E. (2004). Generalized hydraulic geometry: Derivation based on a multiscaling formalism. *Water Resources Research*, *40*, W06302. <https://doi.org/10.1029/2003WR002082>
- Dombradi, E., Timar, G., Gabor, B., Sierd, C., & Frank, H. (2007). Fractal dimension estimations of drainage network in the Carpathian-Pannonian system. *Global and Planetary Change*, *58*, 197–213.
- Falconer, K. J. (1990). *Fractal geometry: Mathematical foundations and applications*. Chichester: John Wiley and Sons.
- Falconer, K. J. (1997). *Techniques in fractal geometry*. Chichester: John Wiley and Sons.
- Feder, J. (1988). *Fractals*. New York: Plenum Press.
- Fernández-Pato, J., Caviedes-Voullième, D., & García-Navarro, P. (2016). Rainfall/runoff simulation with 2D full shallow water equations: Sensitivity analysis and calibration of infiltration parameters. *Journal of Hydrology*, *536*, 496–513.
- Gangogadamage, C., Belmont, P., & Fofoula-Georgiou, E. (2011). Revisiting scaling laws in river basins: New considerations across hillslope and fluvial regimes. *Water Resources Research*, *47*, W07508. <https://doi.org/10.1029/2010WR009252>
- Gires, A., Abbes, J.-B., da Silva Rocha Paz, I., Tchiguirinskaia, I., & Schertzer, D. (2018). Multifractal characterisation of a simulated surface flow: A case study with multi-hydro in Jouy-en-Josas, France. *Journal of Hydrology*, *558*, 482–495.
- Gires, A., Tchiguirinskaia, I., Schertzer, D., Ochoa-Rodriguez, S., Willems, P., Ichiba, A., et al. (2017). Fractal analysis of urban catchments and their representation in semi-distributed models: Imperviousness and sewer system. *Hydrology and Earth System Sciences*, *21*(5), 2361–2375.
- Gleason, C. J., & Wang, J. (2015). Theoretical basis for at-many-stations hydraulic geometry. *Geophysical Research Letters*, *42*, 7107–7114. <https://doi.org/10.1002/2015GL064935>
- Godsey, S. E., & Kirchner, J. W. (2014). Dynamic, discontinuous stream networks: Hydrologically driven variations in active drainage density, flowing channels and stream order. *Hydrological Processes*, *28*(23), 5791–5803.
- Gonzalez, R. L., & Pasternack, G. B. (2015). Reenvisioning cross-sectional at-a-station hydraulic geometry as spatially explicit hydraulic topography. *Geomorphology*, *246*, 394–406.
- Halsey, T. C., Jensen, M. H., Kadanoff, L. P., Procaccia, I., & Shraiman, B. I. (1986). Fractal measures and their singularities: The characterization of strange sets. *Phys. Rev. A*, *33*(2), 1141–1151.
- Harte, D. (2001). *Multifractals: Theory and applications* (1st ed.). Boca Raton: C. H. CRC.
- Harten, A., & Hyman, J. M. (1983). Self adjusting grid methods for one-dimensional hyperbolic conservation laws. *Journal of Computational Physics*, *50*(2), 235–269.
- Hirsch, C. (1990). *Numerical computation of internal and external flows. Vol 2: Computation methods for inviscid and viscous flows*. New York: Wiley.
- Hooshyar, M., Kim, S., Wang, D., & Medeiros, S. C. (2015). Wet channel network extraction by integrating LiDAR intensity and elevation data. *Water Resources Research*, *51*, 10,029–10,046. <https://doi.org/10.1002/2015WR018021>
- Hooshyar, M., Singh, A., & Wang, D. (2017). Hydrologic controls on junction angle of river networks. *Water Resources Research*, *53*, 4073–4083. <https://doi.org/10.1002/2016WR020267>
- Hooshyar, M., Wang, D., Kim, S., Medeiros, S. C., & Hagen, S. C. (2016). Valley and channel networks extraction based on local topographic curvature and k-means clustering of contours. *Water Resources Research*, *52*, 8081–8102. <https://doi.org/10.1002/2015WR018479>
- Hou, J., Wang, T., Li, P., Li, Z., Zhang, X., Zhao, J., & Hinkelmann, R. (2018). An implicit friction source term treatment for overland flow simulation using shallow water flow model. *Journal of Hydrology*, *564*, 357–366.
- Howard, A. D. (1994). A detachment-limited model of drainage basin evolution. *Water Resources Research*, *30*(7), 2261–2285.
- Huang, W., Cao, Z., Qi, W., Pender, G., & Zhao, K. (2015). Full 2D Hydrodynamic modeling of rainfall-induced flash flood. *Journal of Mountain Science*, *12*(5), 1203–1218.
- Ijjasz-Vasquez, E. J., Bras, R. L., & Rodriguez-Iturbe, I. (1993). Hack's relation and optimal channel networks: The elongation of river basins as a consequence of energy minimization. *Geophysical Research Letters*, *20*(15), 1583–1586.
- Ijjasz-Vasquez, E. J., Rodriguez-Iturbe, I., & Bras, R. L. (1992). On the multifractal characterization of river basins. *Geomorphology*, *5*, 297–310.
- Juez, C., Lacasta, A., Murillo, J., & García-Navarro, P. (2016). An efficient GPU implementation for a faster simulation of unsteady bed-load transport. *Journal of Hydraulic Research*, *54*(3), 275–288.
- Kamer, Y., Ouillon, G., & Sornette, D. (2013). Barycentric fixed-mass method for multifractal analysis. *Physical Review E*, *88*(022922).
- Karlinger, M. R., Over, T. M., & Troutman, B. M. (1994). Relating thin and fat-fractal scaling of river-network models. *Fractals*, *2*(4), 557–656.
- Karlinger, M. R., & Troutman, B. M. (1992). Fat fractal scaling of drainage networks from a random spatial network model. *Water Resources Research*, *28*(7), 1975–1981.
- Lashermes, B., Fofoula-Georgiou, E., & Dietrich, W. E. (2007). Channel network extraction from high resolution topography using wavelets. *Geophysical Research Letters*, *34*, L23S04. <https://doi.org/10.1029/2007GL031140>

- Lawrence, D. S. (2007). Analytical derivation of at-a-station hydraulic-geometry relations. *Journal of Hydrology*, 334(1-2), 17–27.
- Le, P. V. V., & Kumar, P. (2014). Power law scaling of topographic depressions and their hydrologic connectivity. *Geophysical Research Letters*, 41, 1553–1559. <https://doi.org/10.1002/2013GL059114>
- Leopold, L. B., & Muddock, T. (1953). The hydraulic geometry of stream channels and some physiographic implications (252). Washington, DC: US Geol. Surv. Prof. Pap.
- Liang, D., Özgen, I., Hinkelmann, R., Xiao, Y., & Chen, J. M. (2015). Shallow water simulation of overland flows in idealised catchments. *Environmental Earth Sciences*, 74(11), 7307–7318.
- Limaye, A. B. (2017). Extraction of multithread channel networks with a reduced-complexity flow model. *Journal of Geophysical Research: Earth Surface*, 122, 1972–1990. <https://doi.org/10.1002/2016JF004175>
- Macchione, F., Costabile, P., Costanzo, C., & De Lorenzo, G. (2019). Extracting quantitative data from non-conventional information for the hydraulic reconstruction of past urban flood events. A case study. *Journal of Hydrology*, 576, 443–465.
- Macchione, F., Costabile, P., Costanzo, C., & De Santis, R. (2019). Moving to 3-D flood hazard maps for enhancing risk communication. *Environmental Modelling & Software*, 111(1), 510–522.
- Mach, J., Mas, F., & Sagués, F. J. (1995). Two representations in multifractal analysis. *Journal of Physics A: Mathematical and General*, 28, 5607–5622.
- Mandelbrot, B. B. (1982). *The fractal geometry of nature*. N.Y., USA: Freeman and Co.
- Mantilla, R., Gupta, V. K., & Troutman, B. M. (2012). Extending generalized Horton laws to test embedding algorithms for topologic river networks. *Geomorphology*, 151–152, 13–26.
- Meneveau, C., & Sreenivasan, K. (1991). The multifractal nature of turbulent energy dissipation. *Journal of Fluid Mechanics*, 224, 429–484.
- Mersel, M. K., Smith, L. C., Andreadis, K. M., & Durand, M. T. (2013). Estimation of river depth from remotely sensed hydraulic relationships. *Water Resources Research*, 49, 3165–3179. <https://doi.org/10.1002/wrcr.20176>
- Montgomery, D. R., & Dietrich, W. E. (1988). Where do channels begin? *Nature*, 336(6196), 232–234.
- Montgomery, D. R., & Foufoula-Georgiou, E. (1993). Channel network source representation using digital elevation models. *Water Resources Research*, 29(12), 3925–3934.
- Nardi, F., Vivoni, E. R., & Grimaldi, S. (2006). Investigating a floodplain scaling relation using a hydrogeomorphic delineation method. *Water Resources Research*, 42, W09409. <https://doi.org/10.1029/2005WR004155>
- Nguyen, P., Thorstensen, A., Sorooshian, S., Hsu, K., AghaKouchak, A., Sanders, B., et al. (2016). A high resolution coupled hydrologic-hydraulic model (HiResFlood-UCI) for flash flood modeling. *Journal of Hydrology*, 541, 401–420.
- O'Callaghan, J. F., & Mark, D. A. (1984). The extraction of the drainage networks from digital elevation data. *Lecture Notes in Computer Science*, 28, 323–344.
- Olsen, L. (1995). A multifractal formalism. *Advances in Mathematics*, 116, 82–195.
- Orlandini, S., & Moretti, G. (2009). Determination of surface flow paths from gridded elevation data. *Water Resources Research*, 45, W03417. <https://doi.org/10.1029/2008WR007099>
- Orlandini, S., Moretti, G., Franchini, M., Aldighieri, B., & Testa, B. (2003). Path-based methods for the determination of nondispersive drainage directions in grid-based digital elevation models. *Water Resources Research*, 39(6), 1144. <https://doi.org/10.1029/2002WR001639>
- Orlandini, S., Moretti, G., & Gavioli, A. (2014). Analytical basis for determining slope lines in grid digital elevation models. *Water Resources Research*, 50, 526–539. <https://doi.org/10.1002/2013WR014606>
- Orlandini, S., Tarolli, P., Moretti, G., & Dalla Fontana, G. (2011). On the prediction of channel heads in a complex alpine terrain using gridded elevation data. *Water Resources Research*, 47, W02538. <https://doi.org/10.1029/2010WR009648>
- Passalacqua, P., Belmont, P., Staley, D. M., Simley, J. D., Arrowsmith, J. R., Bode, C. A., et al. (2015). Analyzing high resolution topography for advancing the understanding of mass and energy transfer through landscapes: A review. *Earth-Science Reviews*, 148, 174–193.
- Passalacqua, P., Trung, T. D., Foufoula-Georgiou, E., Sapiro, D., & Dietrich, W. E. (2010). A geometric framework for channel network extraction from LiDAR: Nonlinear diffusion and geodesic paths. *Journal of Geophysical Research*, 115, F01002. <https://doi.org/10.1029/2009JF001254>
- Pelletier, J. D. (2013). A robust, two-parameter method for the extraction of drainage networks from high-resolution digital elevation models (DEMs): Evaluation using synthetic and real-world DEMs. *Water Resources Research*, 49, 75–89. <https://doi.org/10.1029/2012WR012452>
- Perron, J. T., Richardson, P. W., Ferrier, K. L., & Lapôtre, M. (2012). The root of branching river networks. *Nature*, 492, 100–103. <https://doi.org/10.1038/nature11672>
- Petaccia, G., Leporati, F., & Torti, E. (2016). OpenMP and CUDA simulations of Sella Zerbino Dam break on unstructured grids. *Computational Geosciences*, 20(5), 1123–1132.
- Pirotti, F., & Tarolli, P. (2010). Suitability of LiDAR point density and derived landform curvature maps for channel network extraction. *Hydrological Processes*, 24(9), 1187–1197.
- Rigon, R., Rinaldo, A., Rodriguez-Iturbe, I., Bras, R. L., & Ijjasz-Vasquez, E. J. (1993). Optimal channel networks: A framework for the study of river basin morphology. *Water Resources Research*, 29, 1635–1646.
- Rinaldo, A., Marani, A., & Rigon, R. (1991). Geomorphological dispersion. *Water Resources Research*, 27(4), 512–535.
- Rinaldo, A., Rodriguez-Iturbe, I., & Rigon, R. (1998). Channel networks. *Annual Review of Earth and Planetary Sciences*, 26, 289–327.
- Rinaldo, A., Rodriguez-Iturbe, I., Rigon, R., Bras, R. L., Ijjasz-Vasquez, E. J., & Marani, A. (1992). Minimum energy and fractal structures of drainage networks. *Water Resources Research*, 28, 2183–2195.
- Rodriguez-Iturbe, I., Marani, M., Rigon, R., & Rinaldo, A. (1994). Self-organized river basin landscapes: Fractal and multifractal characteristics. *Water Resources Research*, 30(12), 3531–3539.
- Rodriguez-Iturbe, I., & Rinaldo, A. (1997). *Fractal river basins, chance and self-organization*. New York: Cambridge University Press.
- Roe, P. L. (1981). Approximate Riemann solvers, parameter vectors, and difference schemes. *Journal of Computational Physics*, 43(2), 357–372.
- Saa, A., Gaseò, G., Grau, J. B., Antòn, J. M., & Tarquis, A. M. (2007). Comparison of gliding box and box-counting methods in river network analysis. *Nonlinear Processes in Geophysics*, 14(5), 603–613.
- Sangireddy, H., Stark, C. P., Kladzyk, A., & Passalacqua, P. (2016). GeoNet: An open source software for the automatic and objective extraction of channel heads, channel network, and channel morphology from high resolution topography data. *Environmental Modelling & Software*, 83, 58–73.
- Schroeder, M. (1996). *Fractals, chaos, power laws*. New York: W. H. Freeman and Company.
- Schubert, J. E., Sanders, B. F., Smith, M. J., & Wright, N. G. (2008). Unstructured mesh generation and land cover-based resistance for hydro-dynamic modeling of urban flooding. *Advances in Water Resources*, 31, 1603–1621.
- Shelef, E., & Hilley, G. E. (2013). Impact of flow routing on catchment area calculations, slope estimates, and numerical simulation of landscape development. *Journal of Geophysical Research: Earth Surface*, 118, 2105–2123. <https://doi.org/10.1002/jgrf.20127>

- Shin, S., & Paik, K. (2017). An improved method for single flow direction calculation in grid digital elevation models. *Hydrological Processes*, 31(8), 1650–1661.
- Simons, F., Busse, T., Hou, J., Özgen, I., & Hinkelmann, R. (2014). A model for overland flow and associated processes within the hydroinformatics modeling System. *Journal of Hydroinformatics*, 16, 375–391.
- Singh, J., Altinakar, M. S., & Ding, Y. (2015). Numerical modeling of rainfall-generated overland flow using nonlinear shallow water equations. *Journal of Hydrologic Engineering*, 20(8), 04014089.
- Sofia, G., Tarolli, P., Cazorzi, F., & Dalla Fontana, G. (2015). Downstream hydraulic geometry relationships: Gathering reference reach-scale width values from LiDAR. *Geomorphology*, 250, 236–248.
- Stephenson, D., & Meadows, M. E. (1986). *Kinematic hydrology and modeling*. Dev. Water Sci. (Vol. 26). Amsterdam; New York: Elsevier.
- Stewardson, M. (2005). Hydraulic geometry of stream reaches. *Journal of Hydrology*, 306(1-4), 97–111.
- Strahler, A. N. (1975). *Physical geography* (4th ed.). New York: Wiley.
- Tarboton, D. G. (1997). A new method for the determination of flow directions and upslope areas in grid digital elevation models. *Water Resources Research*, 33(2), 309–319.
- Tarboton, D. G., Bras, R. L., & Rodriguez-Iturbe, I. (1991). On the extraction of channel networks from digital elevation data. *Hydrological Processes*, 5, 81–100.
- Tarolli, P. (2014). High-resolution topography for understanding Earth surface processes: Opportunities and challenges. *Geomorphology*, 216, 295–312.
- Tarolli, P., & Dalla Fontana, G. (2009). Hillslope-to-valley transition morphology: New opportunities from high resolution DTMs. *Geomorphology*, 113(1-2), 47–56.
- Tayfur, G., Kavvas, M. L., Govindaraju, R. S., & Storm, D. E. (1993). Applicability of St. Venant equations for two-dimensional overland flows over rough infiltrating surfaces. *Journal of Hydraulic Engineering*, 119(1), 51–63.
- Vaccondio, R., Dal Palù, A., Ferrari, A., Mignosa, P., Aureli, F., & Dazzi, S. (2017). A non-uniform efficient grid type for GPU-parallel shallow water equations models. *Environmental Modelling & Software*, 88, 119–137.
- Veneziano, D., & Iacobellis, V. (1999). Self-similarity and multifractality of topographic surfaces at basin and subbasin scales. *Journal of Geophysical Research*, 104, 12,797–12,812. <https://doi.org/10.1029/1999JB900083>
- Veneziano, D., & Niemann, J. D. (2000). Mathematical conditions and physical origin. *Water Resources Research*, 36, 1923–1936. <https://doi.org/10.1029/2000WR900053>
- Wittmann, R., Bungartz, H. J., & Neumann, P. (2017). High performance shallow water kernels for parallel overland flow simulations based on FullSWOF2D. *Computers & Mathematics with Applications*, 74, 110–125.
- Wohl, E. (2018). The challenges of channel heads. *Earth-Science Reviews*, 185, 649–664.
- Xia, X., & Liang, Q. (2018). A new efficient implicit scheme for discretising the stiff friction term in the shallow water equations. *Advances in Water Resources*, 117, 87–97.
- Xia, X., Liang, Q., Ming, X., & Hou, J. (2017). An efficient and stable hydrodynamic model with novel source term discretization schemes for overland flow and flood simulations. *Water Resources Research*, 53, 3730–3759. <https://doi.org/10.1002/2016WR020055>
- Yeh, G.-T., Shih, D.-S., & Cheng, J.-R. C. (2011). An integrated media integrated processes watershed model. *Computers & Fluids*, 45, 2–13.